Title
Ionic and Electronic Transport in Nanoscale Systems /

Author
Wilson, James Michael

Publication Date
2013

Peer reviewed|Thesis/dissertation

UNIVERSITY OF CALIFORNIA, SAN DIEGO

Ionic and Electronic Transport in Nanoscale Systems

A dissertation submitted in partial satisfaction of the
requirements for the degree
Doctor of Philosophy

in

Physics with a Specialization in Computational Science

by

James Michael Wilson

Committee in charge:

Professor Massimiliano Di Ventra, Chair
Professor Prabhakar Bandaru
Professor Dimitri Basov
Professor Clifford Kubiak
Professor Doug Smith

2013

The dissertation of James Michael Wilson is approved, and it is acceptable in quality and form for publication on microfilm and electronically:

_____

_____

_____

_____

_____
Chair

University of California, San Diego

2013

EPIGRAPH

"When I use a word," Humpty Dumpty said in a rather scornful tone,
"it means just what I choose it to mean–neither more nor less."
—Lewis Carroll

TABLE OF CONTENTS

LIST OF FIGURES

LIST OF TABLES

ACKNOWLEDGEMENTS

I would like to thank my advisor, Professor Massimiliano Di Ventra, whose guidance and insight have been essential to achieving this work. He has been deeply involved in all aspects of this research, and his attentive support and responsiveness has been much appreciated.

I would like to thank my collaborator, Mike Zwolak. He has been a pleasure to work with, and has much insight in ion transport. I would also like to thank group members: Heiko Appel, Matt Krems, Dibyendu Roy, Alex Stotland, Sebastian Diaz, and Ben Migliori. They have given and asked many helpful comments and questions.

Finally, I would like to especially thank Paul Boynton, for many helpful discussions and conversations. He has been a wonderful person to share an office with, and having him nearby to quickly discuss a new idea greatly helped my understanding of complex problems.

Chapter 5 is in part a reprint of the material as it appears in M. Zwolak, J. Wilson, and M. Di Ventra, "Dehydration and Ionic Conductance Quantization in Synthetic Nanopores", *J. Phys.: Condens. Matter*, 22, 454126 (2010). The dissertation author was a co-author of this paper.

Chapter 6 is in part a reprint of the material as it appears in James Wilson and M. Di Ventra, Single-Base DNA Discrimination via Transverse Ionic Transport, *Nanotechnology* 24, 415101 (2013). The dissertation author was the primary investigator of this paper.

Chapter 7 is in part a reprint of the material as it appears in James Wilson and M. Di Ventra, "Extending the Microcanonical Formalism Through the Stochastic Schrodinger Equation", in preparation (2013). The dissertation author was the primary investigator of this paper.

VITA

2004	B. S. in Physics and Mathematics, Walla Walla University
2004-2007	Physics Teacher, Monterey Bay Academy
2007-2008	Teaching Assistant, Department of Physics, University of California, San Diego
2008-2009	Physics Tutorial Center Coordinator, Department of Physics, University of California, San Diego
2009	M. S. in Physics, University of California, San Diego
2009-2013	Research Assistant, Department of Physics, University of California, San Diego
2013	Ph. D. in Physics, University of California, San Diego

PUBLICATIONS

M. Zwolak, J. Wilson, and M. Di Ventra, "Dehydration and Ionic Conductance Quantization in Synthetic Nanopores", *J. Phys.: Condens. Matter*, 22, 454126 (2010).

Massimiliano Di Ventra, Matt Krems, James Wilson, and Yuriy V. Pershin, "DNA characterization by transverse electrical current in a nanochannel",*Methods in Molecular Biology*, Vol 870 (2012).

O. Khatib, J. D. Yuen, J. Wilson, et al, "Infrared spectroscopy of narrow gap donor-acceptor polymer-based ambipolar transistors", *Phys Rev B*, 86, 195109 (2012)

James Wilson and M. Di Ventra, "Extending the Microcanonical Formalism Through the Stochastic Schrodinger Equation, in preparation (2013).

James Wilson and M. Di Ventra, Single-Base DNA Discrimination via Transverse Ionic Transport", *Nanotechnology* 24, 415101 (2013).

ABSTRACT OF THE DISSERTATION

Ionic and Electronic Transport in Nanoscale Systems

by

James Michael Wilson

Doctor of Philosophy in Physics with a Specialization in Computational Science

University of California, San Diego, 2013

Professor Massimiliano Di Ventra, Chair

In this dissertation, I examine ion transport in nanopores, which has been met with increased interest in the last two decades due to its ability to detect DNA. I start with an overview of the properties of DNA and ionic transport in nanopores. I will explain some of the methods used for measuring ionic transport in nanopores using molecular dynamics. I will also discuss microcanonical formalism of electronic transport in nanoscale systems. This method of studying electronic transport is increasing in popularity as the emphasis on nanoscale devices increases. I will also discuss an open quantum systems approach to extending this formalism.

Next, I will discuss the effect that small pore size has on the ionic conductance of that pore. A previous study predicted that as the radius of a nanopore increases, the conductance of a nanopore will exhibit discrete jumps when the

radius of the pore is comparable to the radius of hydration layers around the current-carrying ions. I extend this prediction to different ion species, and conclude that it will be easier to detect these features by using divalent ions. I also look at what effect membrane dielectric choice and noise has on the current using the proposed theory.

I will continue by proposing a new method of DNA sequencing, consisting of measuring the ionic current in a nanochannel that is transverse to a second, intersecting, nanochannel containing a single strand of DNA. The DNA will be pulled through its channel and modulations in the ionic current will allow the identities of the DNA bases to be deduced. A molecular dynamics model was used to test the feasibility of this method of sequencing.

Finally, I will discuss a method for modeling electronic current in nanoscale systems. I use an open quantum systems approach (stochastic Schrodinger equation) to model a specific bath that has properties similar to how one would expect a battery to operate. This is used to increase the amount of time a system can exist in a quasi-steady current carrying state within the microcanonical formalism.

Chapter 1

Introduction

From nanolithography that supports new generations of microchips to nanotubes that are used in detectors for scanning-tunneling microscopy, advances in the understanding of nanoscale systems are allowing some of the most important advances in technology. Nanoscale devices showcase the differences that are present when the scale of the system shrinks drastically. Instead of using the bulk properties of the materials, the individual atoms become important for transport, therefore new methods must be used to model these atomic scale systems.

It has been over 80 years since the discovery that our genetic information is held in a linear string of deoxyribonucleic acid (DNA) [1]. Each strand pairs with a complementary strand such that within each of our cells (with some minor exceptions), we hold a complete blueprint for our physical makeup in a double-helical configuration. Almost 40 years ago, we were first shown a reliable method of recovering that data[2, 3], but the first full human genome was not sequenced until a little over 10 years ago [4]. To date, we still have not devised a method of sequencing a genome in a fast, cheap, and reliable way.

I will begin with an overview of DNA and the methods that use nanopores to sequence DNA in Chapter 2. Nanopores confine the DNA to a small space, which makes the process of detecting differences between the bases easier. Detectors can be set up next to the pore and the DNA travels by the detector, thus simplifying the process of detection. Making good use of the strengths of nanopores in this regard requires knowing some of the properties of nanopores, therefore in Chapter

2 I discuss the properties of ionic transport in nanopores.

Because much of the work in this dissertation involves the simulation of nanoscale systems with molecular dynamics, I use Chapter 3 to explain some of the theory behind classical molecular dynamics, and how a typical simulation is prepared and run. I first explain the forces that are simulated in the molecular dynamics code (NAMD). Each of these forces add another term to the equations of motion of the system, and it is instructive to see what types of interactions are taken into consideration. Even though classical molecular dynamics does not employ quantum mechanics directly in its simulations, the effects of quantum mechanics on the forces between atoms and molecules appear within its force terms. After this, I explain the process of creating a nanopore in silico. Finally, I describe the process of running the simulations and each of the equilibrations that are required.

In Chapter 4 I give an overview of the Microcanonical Formalism used as a method of calculating electronic current in nanoscale systems. The entire system is treated quantum mechanically in this formalism, and electronic interactions can be studied. I discuss the different phases of the simulation in this section, and then explain generally how I extend this with the stochastic Schrodinger equation in Chapter 7.

Chapter 6 outlines a novel method of sequencing DNA. It proposes exploiting the transverse ionic current passing by a single strand of DNA to discriminate between bases within the strand. The ionic current flowing in the same direction as the DNA has been previously measured and researched, but difficulty has been found in using this information for practical sequencing. One of the problems with using longitudinal ionic conductance as a way to sequence is that the current necessarily flows by many DNA bases within the nanopore. Each base affects the ions as they flow by, but the resultant current is then a non-trivial convolution of all of these effects. *Transverse* ionic current flows transverse to the DNA strand and thus only "sees" 1 or a small number of bases. I then calculate the transverse ionic current for each base in such a system using a full, all atom molecular dynamics simulation. I then compare the distributions of this current and conclude that

the currents are different enough to make discrimination between the bases using transverse ionic conductance possible.

Chapter 5 expands on a theory of ionic current for small diameter nanopores. The ionic conductance through a nanopore for sufficiently large pores is proportional to cross-sectional area. However, ions in aqueous solution do not move alone through water, but also drag along hydration shells of water as they move. If the nanopore is smaller than a certain effective diameter, the hydration layers attached to each ion must break to allow the ion to pass through the pore. This causes the current to drop off sharply as the pore size drops below the size of the hydration layers. The theory was originally proposed in Ref [5]; this chapter expands on this theory. First, by using divalent ions, which have sharper current features, The possibility of experimental verification is increased. Second, I explore the effect that different pore materials have on the conductance of the pore. Third, I discuss different types of noise and their effect on the current.

In Chapter 7 I explore a method of simulating a battery within the microcanonical formalism of transport. One of the limitations of the microcanonical formalism is the limited amount of time that the system stays in a quasi steady state. I use an open quantum systems approach, namely the stochastic Schrodinger equation, to simulate the effect that a battery has on a circuit. This allows the system to remain in a quasi steady state indefinitely.

Chapter 2

DNA and Ionic Currents

2.1 DNA Form and Function

Methods of sequencing DNA is an exciting area of study. DNA is a large molecule that is present in the nuclei of our cells. It governs the production of the proteins that are the machinery of our bodies. Specifically, DNA consists of four different nucleobases: adenine (A), cytosine (C), guanine (G), and thymine (T), each attached to a deoxyribose sugar. Each of these bases (A,C,G,T) can be attached to any other by connecting their two deoxyriboses with a phosphate group. A long string of these forms single-stranded DNA, with the deoxyribose and phosphate groups making up the backbone of the DNA. Furthermore, each A pairs with T, and each C pairs with G through hydrogen bonding. This allows a single stranded piece of DNA to pair with its complementary strand forming double-stranded DNA.

This double-stranded DNA is held inside the nucleus of almost all cells in the human body (red blood cells, and a few other specialized cells excepted). Through a several-step process, a protein is made from the code in the DNA. First, the DNA is unzipped. Next, an RNA polymerase makes a copy of the DNA out of RNA. The strand of RNA then finds its way to a ribosome, which attaches another amino acid to a chain of amino acids for every three bases the RNA contains. For instance if the first three bases of the RNA are GCC, an alanine starts off the chain, and if the next three are CGA, an arginine is attached to the first alanine.

Each of the other 20 amino acids correspond to one or more 3-base codons. In this way, a long string of DNA can ultimately be translated into a string of amino acids, which then fold into proteins.

The interplay of the various proteins produced in the cells cause the differences in life we see around us. For instance, a person's eye color is directly related to the presence or absence of a few proteins expressed in the cells making up the iris of the eye. These proteins, in turn, are present only when the particular string of bases that make up those proteins are present in that person's DNA. Similarly, having a particular string of bases in their DNA can cause a person to have an increased chance of getting breast cancer, while having another gene can cause a person to have an increased chance of coronary artery disease. There exist tests to check for some of these known genes, but they remain expensive, and specific. It wouldn't be reasonable to take one of the tests unless there were independent evidence that the patient is at risk.

Conversely, if a person were to have their entire genome sequenced, the genetic information would reveal the results of all known genetic tests. This is not often done in a clinical setting because of the immense cost in sequencing an entire genome. With recent advances in sequencing technology, companies such as Illumina and Pacific Biosciences offer full genome sequencing in the $5,000 to $10,000 dollar range, but even though the cost has been decreasing at a significant rate in recent years, it still hasn't reached a level where a health care provider can expect this kind of genetic information from many patients. Once the cost has decreased to where it is cost effective for every person to have their full genome sequenced, healthcare would become customized to the individual. This would enable what is called *personalized* medicine.

Personalized medicine would allow those people that have a statistical likelihood of acquiring a disease late in life to learn about this likelihood early enough to take mitigating measures. For instance, knowing that a person is likely to acquire coronary artery disease would allow that person to take measures to lower his or her cholesterol levels early in life to not allow the disease to progress. Knowing of a predisposition for cancer would allow for more targeted testing throughout life,

which would increase the chance of detecting the cancer early and thus increase the chance of favorable outcomes.

2.2 Nanopores

Work has been done on novel methods to sequence DNA, with much research in nanopore methods. A nanopore is a hole with a diameter on the order of a few nanometers that crosses a membrane separating two water reservoirs. When a piece of DNA is added to one of the reservoirs, and an electric field is applied crossing the membrane, the DNA will find the pore and translocate to the other side of the membrane. The first example of this process was performed in 1996 by using an α-hemolysin pore embedded in a lipid membrane [6]. This was the first work to demonstrate the ability to use a nanopore as a kind of Coulter-counter by measuring the ionic current through the pore. When a DNA molecule was in the process of passing through the pore, the ionic current would be diminished. This allowed researchers to use data such as the time of depressed current to estimate the length of the DNA strand passing through. It was initially thought that by simply measuring the ionic current through the pore at the same time as the DNA translocates through the pore, there might be enough information to sequence the strand of DNA, but so far this has not panned out. Longitudinal ionic current (current in the direction the DNA is traveling) has not been sufficient to sequence DNA in part because of the finite size of the pore. In even very short pores, there are on the order of tens of DNA bases in the pore at once, and the ionic current "sees" all of these bases as it passes through the pore.

It has been shown that it is possible to sequence a single base of DNA using longitudinal ionic current, but it has required a very careful set up [7, 8]. There must be a very small restriction within the pore, and the base to be sequenced must be immobilized very carefully so that it lies directly at the restriction. The small restriction is achieved by using a modified Mycobacterium smegmatis porin A (MspA, a biological pore produced by mycobacteria) pore, and the tight control is accomplished by using specially engineered strands of DNA that contain a hairpin

at one end. The DNA enters the pore and the hairpin stops the translocation leaving a specific base at the restriction of the pore. Very fine continuous control of the DNA molecule has been difficult to achieve thus far, but has been an active area of research [9, 10].

Alternative methods of sequencing [11, 12, 13], using electrodes embedded in the sides of the nanopore have shown some promise as of late [14]. Because the electrodes are placed transverse to the DNA strand, the tunneling current passes mostly through just one base at a time. This allows the experimenter to discriminate individual bases from one another. This method requires a different method of pore creation. Rather than borrowing a pore from nature, synthetic pores can be made from SiO_2 or Si_3N_4. This allows more control over the shapes of pores that can be used, however it gives up some of the consistency that comes from biological pores.

2.3 Synthetic Nanopores

Synthetic pores start out as a uniform membrane of Si_3N_4. Then a hole is punched through the material using a focused ion beam (FIB). The hole that is created is much too large to be used as a nanopore as it will have a diameter of about 60nm. The next step is to slowly shrink the hole down. The group of Li and Golovchenko [15] use a gas of Ar^+ ions to drive diffusion processes that decrease the diameter of the hole. As the hole decreases in size, the current of Ar^+ ions decrease in proportion to the area of the pore, so they stop the process when the current of Ar^+ ions decreases to a predetermined value.

Alternatively, a large pore in SiO_2 can be shrunk by bombarding with an electron beam as per [16]. The process uses a transmission electron microscope (TEM) to supply an electron beam with a resolution of about 0.2nm, so the size of the pore can be monitored visually until it reaches the chosen size. Furthermore, the closing of the pore happens at around 0.3 nm/min, which gives plenty of time to cut off the electron beam at the correct pore diameter.

One of the difficulties in using synthetic nanopores is that often nothing

is known about the surface of the nanopore after its creation. Because individual atoms are apparent at the nanometer length scales, the pore is unlikely to be completely smooth, and there may be a large surface charge. A surface charge in the pore will affect DNA translocation, possibly causing the DNA to "stick" to the walls. Furthermore, a charged pore would cause an increase in the ionic current passing through the pore. This is thought to occur because it increases the local ionic density in the pore, and once in the pore, ions are more likely to cause current. In the works contained in this dissertation, the nanopores are cut out of crystalline Si_3N_4, and they will not be necessarily cylindrically symmetric. This may be true of pores in experiment, but as the pore formation is thought to be a diffusive process, the crystal structure near the surface will not be as rigid and will instead be disordered.

The Bohr radius $a_0 \approx 0.53$Å, to an order of magnitude, approximates the radius of an average atom, so we see that a nanopore with a diameter of 2.0nm is only 20 atoms across. Because individual atoms are a non-negligible size within nanopores, ionic current dynamics differ from those in larger sized structures. Furthermore, with typical ionic concentrations of 1M, the mean distance between ions in water (assuming complete dissociation of monovalent ions) is 9.4Å. Therefore for a small pore, it is likely to see only 1 ion within the pore at one time.

2.4 Ions in Water

When one models an ion in water, a dielectric medium, we see that the electric field surrounding the ion dies off much faster than if the ion were in vacuum. This is the normal effect that a dielectric medium has, and water has a dielectric constant of about 80. However, when looking at *very* short distances around the ion, the properties of individual water molecules start to play a role. Water is a dielectric because of its dipole moment and its ability to rotate in an electric field. Over length scales of tens of nanometers, the water molecules are very small compared to the distances measured, and they are not constrained so that the effects of individual water molecules average out to attenuating the electric field

at every point by a factor of 1/80. Very close to an ion, however, one can think of individual water molecules being discrete objects, and the local electric field will be varying wildly.

An ion in a water solution will attract nearby water molecules with a charge-dipole interaction. Only a certain number of water molecules can fit in the area directly surrounding the ion. Because of this, if we time-average the positions of the water molecules surrounding the ion, we find that the water molecules will form a hydration layer [5] around the ion. Because of the attraction between the ion and these water molecules in the hydration layer, it would take energy to pull one of these water molecules out of the hydration layer. Water is neutrally charged, so if we package the ion with this first hydration layer, we can think of this package as a quasiparticle with the same charge as that of the ion, but with a larger radius. This quasiparticle then attracts water molecules just as the bare ion did, thus defining a second hydration layer. This process can be repeated, but after 2 to 3 hydration layers, the bonding energy of the hydration layer becomes close to the thermal fluctuations, and the layer is not visible.

For large sized pores with diameter above 10nm, the ionic conductance of the pore is directly proportional to the cross-sectional area of the pore. However, for pores around 2nm diameter and smaller, the microscopic configuration of the water molecules around the ion matters. When the ion enters the pore, the hydration layers do not have enough space to stay around the ion and must be shed. Because the shedding of the hydration layers costs energy, it is predicted that the ionic conductance of the pore will drop faster than the cross-sectional area, in a phenomenon called quantized ionic conductance.

Finally, in chapter 6 of this dissertation, I discuss the use of transverse *ionic* conductance in nanopores to discriminate DNA bases in single-stranded DNA. This requires a novel configuration of a nanopore as two intersecting nanopores must be present in the membrane, and there must be four water reservoirs connected to these nanopores. A recent attempt at producing such a device is described in [17]. It was accomplished by first creating a microfluidic structure patterned into the system by photolithography in SiO_2. The nanochannels are then milled into

the system using FIB. Once the nanochannels are cut into the membrane, a SiO_2 coverslip is then fused over the top of channel structure, sealing it in.

Chapter 3

Molecular Dynamics

Classical molecular dynamics (MD) simulations are very well suited for studying pores of nanoscale dimensions. Inter-atomic distances within a nanopore system are on the order of $\sim 1\,\text{Å}$, meaning an all-atom simulation covering a small nanopore must contain more than a thousand atoms. Full, many-body, quantum mechanical simulations are not feasible for timescales involving water movement and ionic currents, i.e. in the femtosecond to nanosecond range. One can make certain assumptions and use Time-Dependent Density Functional Theory (TDDFT), but generally one can only simulate a few hundred atoms up to femtoseconds of time at great computational expense. This would leave out much of the complex interplay between the motion of water molecules and ions in the pore because these effects happen at longer timescales.

Classical molecular dynamics simulations do not simulate the motion of electrons. This is justified in the case that atoms have electrons in deep potential wells that are separated from each other by a great distance, i.e. tight-binding. This distance between atoms means that there is a very small probability of electrons tunneling between the nuclei, and the motion of the electrons doesn't have much effect on the motion of nuclei. By ignoring the electron motion, we can make a few assumptions that greatly simplify the simulations. Firstly, because ions are on the order of a thousand times heavier than electrons, it follows that ions react a thousand times slower to forces, and we can safely increase the timestep size by a factor of a thousand. This is not to say that the effect of the electrons

has disappeared from the simulation completely. The electrons are treated phenomenologically by adding a Lennard-Jones type term to the force equation, and also by adding partial charges to atoms within molecules with known intrinsic dipole moments.

The equation of motion for classical MD is Newton's second law:

$$m_i \ddot{\mathbf{r}}_\mathbf{i} = -\frac{\partial}{\partial \mathbf{r_i}} U_{total}\left(\mathbf{r_1}, \mathbf{r_2}, ...\mathbf{r_N}\right), \; i = 1, 2, ..., N \tag{3.1}$$

where m_i, $\ddot{\mathbf{r}}_\mathbf{i}$ are the mass and position of the ith atom, N is the number of atoms included in the simulation, and U_{total} is the total potential energy from all of the forces acting in the system. The potential function is where the interactions between the atoms enter into the simulation, and it governs the evolution of the system. All of the details that make up how the atoms and ions react to each other (except for chemical reactions) are encapsulated in that equation. For instance, the hydrogen atoms in a water molecule are held at a distance of 0.9572Å from the oxygen atom in our simulations, which are based on the TIP3P [18] model of water. This means that U_{total} contains a bonding term that increases in energy if the atoms vary from this distance.

3.1 Force Field

Let us take a look at the pieces of the force field that come into play when performing an all-atom molecular dynamics simulation. In the absence of any forces in the potential function ($U_{total} = 0$), and with reflective boundary conditions, the system will approximate a 3D non-interacting ideal gas. We then must add forces to U_{total} to more closely approximate the environment within an actual nanopore. The potential can further be separated into two categories: bonded contributions, and non-bonded contributions. The bonded contributions are only included between 2 or more atoms when there exists a chemical bond between those atoms. For example, if we were to study a system that consisted of a single water molecule, there would be a bonded contribution between the oxygen and hydrogen atoms. The non-bonded contributions would primarily affect atoms that are not chemically bonded together. Thus, we would need to add at least two

molecules to our simulation to have an effect from these terms. Next we will look at the bonded contributions to U_{total} in greater depth.

3.1.1 Bonded Contributions to U_{total}

When atoms are covalently bonded together, the force of that bond will be one of the strongest effects on the atom's motion. The bonded atoms will tend to equilibrate to a distance r_{AB}, where atoms i and j are of element A and B respectively. This bond distance will depend on the identity of the two atoms, and the molecule that the atoms are a part of. NAMD then approximates the energy of this bond by using a harmonic potential,

$$U_{bond} = k_{AB} \left(r_{ij} - r_{AB}\right)^2$$

where k_{AB} and r_{AB} are tabulated for each element A and B that will be encountered in the simulation.

Whenever three atoms combine to form a molecule, there is an angle defined between them that is based on the underlying electronic structure of each of the atoms. For instance, water forms an angle of about 105^o between the H-O-H bonds. Because NAMD does not calculate the electronic structure of the atoms, this constraint must be supplied by hand. As before, we assume a quadratic potential

$$U_{angle} = k_{\Theta,ABC} \left(\Theta_{ijk} - \Theta_{ABC0}\right)^2$$

where $k_{\Theta,ABC}$ is the Hooke's Law coefficient for the angular restoring force, and the angle Θ_{ABC} is the equilibrium angle on the connected elements A, B and C.

Finally, when a molecule has at least four atoms in a chain, we will label them as atom A, B, C and D. A molecule containing this chain sometimes prefers a particular angle between the plane made by atoms A, B and C, and the plane made by atoms B, C and D. The angle between these two planes we call the dihedral angle, and within our simulations we add a term to the potential that ascribes a minimum in energy when the preferred dihedral angle is achieved. This term takes two forms depending on the periodicity of this energy minimum. If there is just one stable angle for atoms A, B, C and D to take, then we have a quadratic dependence

of the energy on the angle. However if there is more than one stable dihedral angle (so that the molecule has a minimum of energy in that configuration), the dihedral term takes on a cosine form.

$$U_{dihedral} = \begin{cases} k_{ABCD}\left(1 + \cos\left(n_{ABCD}\psi_{ijkl} + \psi_{ABCD0}\right)\right) & \text{if } n > 0 \\ k_{ABCD}\left(\psi_{ijkl} - \psi_{ABCD0}\right)^2 & \text{if n=0} \end{cases} \tag{3.2}$$

3.1.2 Non-Bonded Contributions to U_{total}

Now we move on to the terms in the potential energy function that affect atoms that are not bonded to one another. For instance, this would refer to a potassium ion in solution interacting with water molecules around it. The first of these non-bonded forces is the Lennard-Jones potential, and a graph of the interaction energy is shown in Figure 3.1. The Lennard-Jones potential is an approximation to the interaction that neutral atoms and molecules feel. It is built up of two parts: the very short range Pauli repulsion, and the longer range attractive London dispersion force. The Lennard-Jones potential contribution to U_{total} then is

$$U_{AB} = -E_{AB}\left[\left(\frac{R_{AB}}{r_{ij}}\right)^{12} - 2\left(\frac{R_{AB}}{r_{ij}}\right)^{6}\right]$$

The energy $-E_{AB}$ is the minimum energy that the Lennard-Jones potential achieves, and the distance R_{AB} is the inter-atomic spacing that minimizes U_{AB}. The attractive r^{-6} term is justified due to its modeling after the London dispersion force, however the repulsive r^{-12} term is used because of its very steep slope, and its ease of calculation as it is just squaring the r^{-6} term. Other approximations are used for the repulsive term, such as an exponential term.

The last potential that we use is the longest range, and therefore the most problematic from an efficiency standpoint. The Coulomb potential only drops off as r^{-1} and is spherically symmetric. The potential is

$$U_A = -k_e\frac{q_i q_j}{r_{ij}}$$

where k_e is the electric constant in appropriate units with distance in angstroms and charge in units of the elementary charge. The charges on atoms i and j are q_i

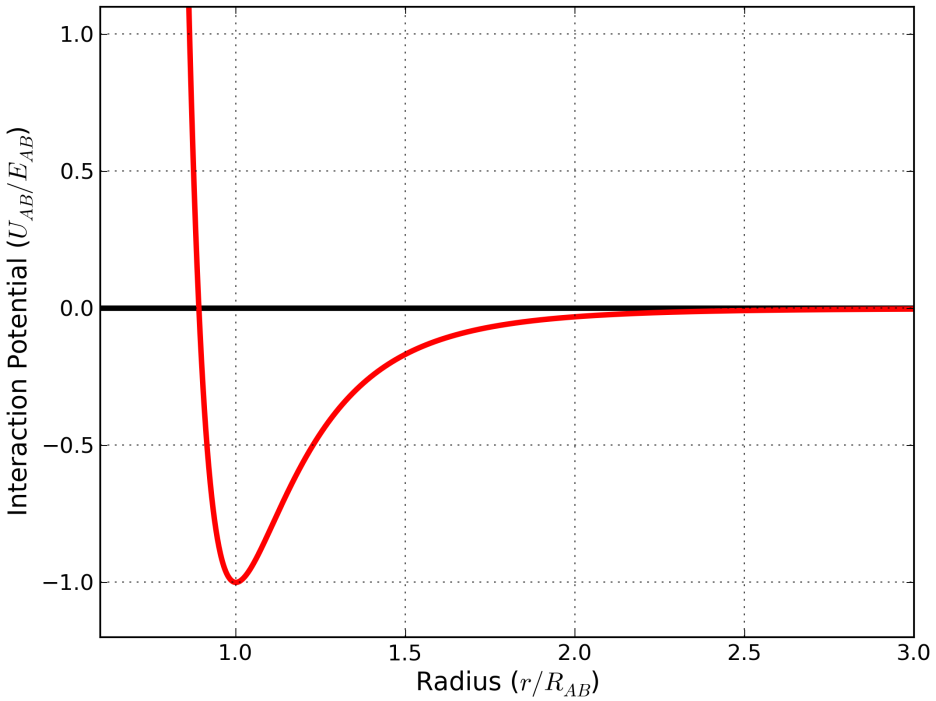

Figure 3.1: A graphical representation of the Lennard-Jones potential, with energy in units of E_{AB}, and distance in units of R_{AB}

and q_j respectively, and the distance between them is r_{ij}. Whenever molecules contain polarities, such as due to differences in electronegativities, the partial charge due to the polarization can be placed on the charges q_i and q_j. This allows the simulation to mimic effects due to dielectric constants. For instance, the hydrogen atoms in the TIP3P model of water[18] each contain a partial charge of $\delta_H = +0.417e$, and the oxygen atom contains a partial charge of $\delta_O = -0.834e$. The r^{-1} potential is very long range and must get dealt with separately to escape the N^2 scaling that would be the case if every atom interacted with every other atom every time step.

3.2 Specifics of NAMD Simulations

The system of simulation generalized above is carried out in specifics by the Nanoscale Molecular Dynamics code (NAMD) [19]. This code can efficiently scale to hundreds of thousands of atoms, and run on hundreds of cores. In the simulations that we run, we use from tens of thousands of atoms, up to the low hundreds of thousands of atoms which allow us with a cluster of about 150 cores to efficiently study dynamics in the nanosecond timescale.

To run a simulation, NAMD requires that the initial conditions and parameters be specified with input files. The first of these input files is the configuration file. This file contains, or points to, all of the remaining data required to run the simulation. It must contain the timestep dt, the geometry of the system, and the names of files describing locations of atoms and the forces between them. Furthermore, it contains all of the information about how the data will be output, and may contain optional features that help describe a more realistic system. The timestep dt of the system is dependent on the mass of the atoms being studied, and the maximum forces expected on those atoms. Because all nanopore simulations of interest to us contain water, and thus hydrogen, we must choose a timestep of $dt = 1$fs or smaller. The geometry of the system is specified directly based on the properties desired in the simulation. The simulations described in this work all use periodic boundary conditions as those would more closely compare to an extended nanopore system. Furthermore, because a nanopore is cylindrically symmetric, hexagonal tiling is more fitting, and thus was used whenever a nanopore was present in the system.

Next, we come to the files that describe the atoms and their interactions in the system. The first file needed is a .pdb or Protein DataBank file. This file lists every atom in the system, its 3D coordinates, and a few more bookkeeping details such as a unique ID number. In theory, this file could be constructed entirely by hand, but in practice it is generally made with the use of a program. The most convenient for use with NAMD is Visual Molecular Dynamics, or VMD [20]. VMD can be scripted to form a nanopore, insert a piece of DNA, solvate the system and insert ions to a specified concentration. Furthermore, many times a .pdb file will

not contain hydrogen atoms in it because they are too small to see with x-ray crystallography. The hydrogen atoms within a simulation are important to the NAMD simulation, VMD will guess at the positions of the hydrogen atoms by using a topology file, and place them in the system. Once the simulation begins, there will be a more thorough energy minimization which will move the hydrogen atoms into their more exact positions.

Once we have a file containing the atom positions, we must also include information describing the interactions between the atoms. The first of these files is called a protein structure file or .psf file. The .psf file contains the atom types, bonds between atoms, atomic masses, and partial charges associated with each atom. This information is generated from general rules included in a CHARMM topology file [21, 22] as interpreted by VMD. The bonds, angles and dihedrals consist only of an unordered listing of all of the atoms involved in each bond, angle and dihedral existent in the simulation. For instance, a simulation of 1 water molecule would contain 2 bonds, 1 angle, and no dihedrals. The parameters of the bonds and angles, i.e. the atom-atom spacing and H-O-H angle would be included in the parameter file.

The parameter file contains the bond distances and bond strengths. This information is recorded from experimental values, or to satisfy a particular constraint on the system. The bonds described in the .psf file must correspond to the bonds in the parameter file. For this reason, the parameter file must be associated with the topology file used to make the .psf file. In the same way, the parameter file contains the bond angles and bond angle stiffness, along with the dihedral angles and their stiffnesses as well.

In conclusion, for a NAMD simulation to run, we must have a valid configuration file, a .pdb file, a corresponding .psf file that was created with a CHARMM topology file, and a parameter file.

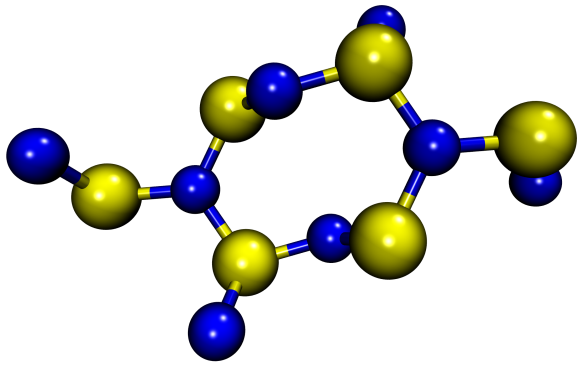

Figure 3.2: One unit of β-phase Si_3N_4. To create a membrane of Si_3N_4, this unit is replicated in the three directions **a**, **b**, and **c** given in the text.

3.2.1 Nanopore Construction for a Molecular Dynamics Simulation

To look at the dynamics inside of a nanopore using molecular dynamics, we must first create a reasonable model of an inorganic nanopore in a computer. We use silicon nitride in the β-phase as the membrane that the nanopore cuts through. A very useful program to accomplish this is Visual Molecular Dynamics (VMD) which is developed alongside NAMD. It uses an easy scripting language, which helps to generate repeatable output, and can use the CHARMM topology files to produce molecular structures that correspond to the information contained in the CHARMM parameter files that NAMD reads.

The first step in creating a nanopore is to build a silicon nitride membrane of the appropriate thickness. This is made by replicating a unit cell (Figure 3.2)

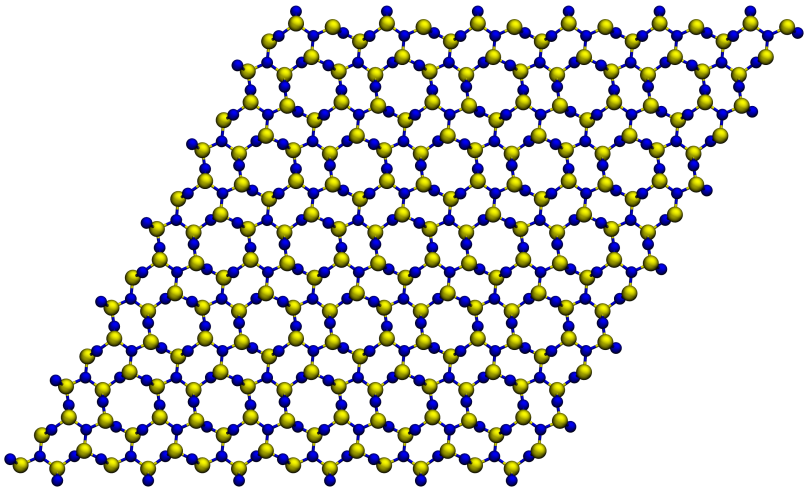

Figure 3.3: This is the unit cell from Figure 3.2 that has been replicated 6 times in both the n_x and n_y directions. The sheet thus created has a rhombus shape that is inefficient for simulating a pore with cylindrical symmetry.

of silicon nitride [23] n_x, n_y and n_z times along the unit cell vectors:

$$\mathbf{a} = 7.595\,[1, 0, 0]$$

$$\mathbf{b} = 7.595\left[1/2, \sqrt{3}/2, 0\right]$$

$$\mathbf{c} = 2.902\,[0, 0, 1]$$

This creates a crystal parallelepiped of β-phase silicon nitride $2.902 \cdot n_z$ angstroms thick in the z direction, and with side lengths of $7.59 \cdot n_x$ and $7.59 \cdot n_y$ angstroms in the $\mathbf{x}$ and $0.5\mathbf{x} + \sqrt{3}/2\mathbf{y}$ directions respectively. This layer of Si_3N_4can then be cut down to the correct dimensions. The membrane is then moved so that the middle of the membrane is placed at the origin of our coordinate system.

Because nanopores in experiments are part of a larger Si_3N_4structure, it more closely mimics experimental conditions to have periodic boundary conditions. This causes the simulation to resemble a large sheet of Si_3N_4rather than

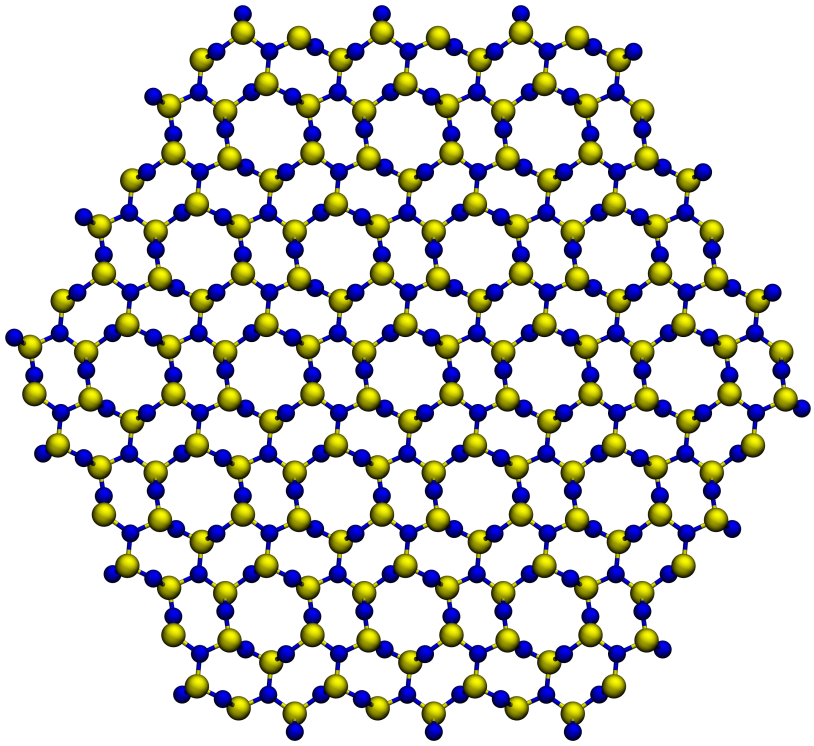

Figure 3.4: The edges of the membrane have been cropped so as to create a hexagonally symmetric shape. By removing the extra atoms at the edge, the simulation box can more closely mimic the cylindrical symmetry of the pore.

the small, isolated pore and water produced by vacuum boundary conditions. The other (image) nanopores that exist in this extended system would not exist in an experimental system, but if the size of the unit cell is large enough, the distance between the pore in the simulation box and the image pores will be quite large, making the effect of one on the other small. Likewise, if the pore is small enough, the pore in the simulation box will see a mostly unbroken sheet of $Si_3N_4$and the image pores will have a small effect.

Furthermore, because of the cylindrical symmetry of the nanopore, it makes sense to use hexagonal tiling in the plane of the membrane, as 6-fold rotational symmetry is closer to cylindrical symmetry than 4-fold rotational symmetry. It is for this reason that the parallelepiped is cut further so that the membrane will be in the right shape for hexagonal tiling. This membrane now looks like Figure 3.4.

Next a pore must be cut in the Si_3N_4. This is accomplished by simply deleting atoms that are contained within the pore. A simple way to create a cylindrical pore would be to use a script in VMD that loops through all of the atoms in the pore. It would then test the inequality

$$x^2 + y^2 < r^2$$

where r is the radius of the pore, and remove all atoms for which that inequality is true. Without much further effort, the formula can be tweaked so that the pore more closely resembles experimentally fabricated pores with a double-conical profile[24, 25]. To apply a 10^o slant to the pore making an hourglass shape, s is defined such that

$$s = r + |z| \cdot \tan 10$$

where r is defined as the minimum pore diameter (existing in the middle of the pore), and z is the z-coordinate of the atom. The script then, for each atom, tests the following inequality

$$x^2 + y^2 < s^2$$

and deletes all atoms for which the inequality holds.

Next, the bonds between the atoms in the pore need to be assigned. To do this, a script enumerates through all of the atoms in the pore, and whenever two of them are closer than 2Å, it assigns a bond to that pair. It similarly creates the angles and then writes all of them to a properly formatted .psf file. Of particular importance are the atoms on the edge of the membrane. Because of the periodic boundary conditions in the x and y directions, the outer atoms in the $Si_3N_4$are directly next to the image atoms in the next cell over. Because of this, the bonds between these atoms are also included in the .psf file.

3.2.2 Adding DNA to the pore

Once the pore is completed, the subject of the study must be added to the pore. For the study on quantized ionic conductance, all that is needed is to add an ion to the center of the pore. This is easily accomplished by just adding the ion

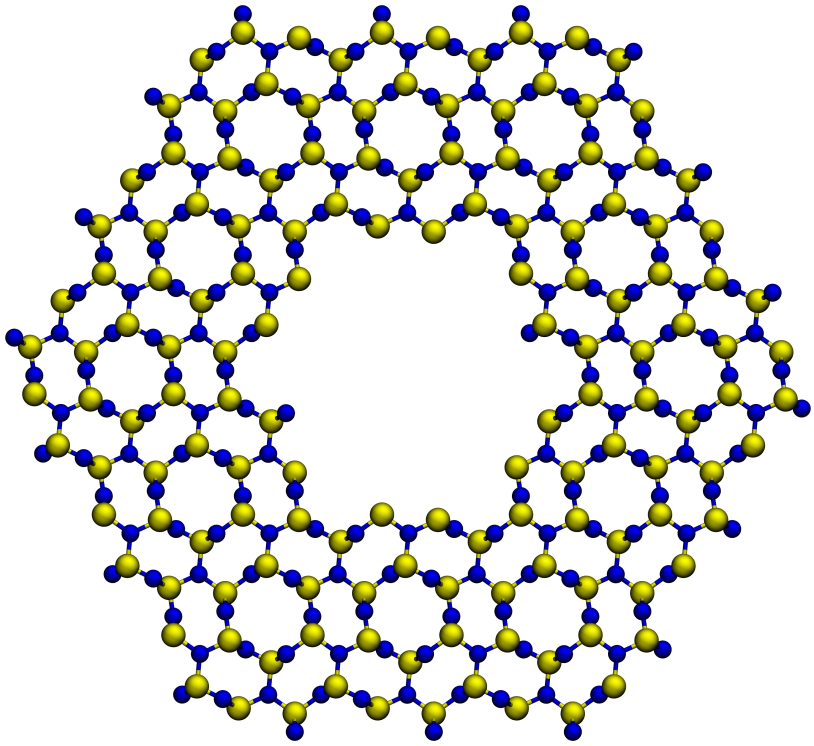

Figure 3.5: After the membrane has been cut into a hexagon as in Figure 3.4, the pore is cut out of the middle. This pore has a radius of 7Å. All atoms with centers closer than 7Å from the center of the membrane have been removed. This leaves an irregular shape due to the crystal structure of the Si_3N_4.

to the .pdb file and .psf file. There must be a counter ion so that the simulation box contains a net neutral charge, but that can be added within the simulation box near the edge. It is more difficult to add a strand of DNA to the pore. First, a strand of single-stranded DNA is cut from a longer strand of double-stranded DNA. This single stranded piece is then equilibrated in a water bath using NAMD. Single-stranded DNA has been known to stretch up to 1.7 times its contour length in B-DNA form[26], and within a nanopore, there is a large force due to electric field that will stretch single-stranded DNA held within it. Therefore, to make the DNA in the pore more realistic, it is pre-stretched in an electric field. It is then aligned with the pore using a script that rotates and translates the DNA so that it is centered in the pore.

3.2.3 Solvating, Adding Ions, and Dielectric Properties

The next step is to add water to the nanopore. This is accomplished by using a script that calls the solvate plugin for VMD. In all cases encountered in this dissertation, if a membrane is included, the membrane is periodic in the x and y directions, but not periodic in the z direction. It is possible to make the membrane periodic in the z direction, e.g. if trying to simulate a very long nanochannel, but several problems arise when trying to simulate a rigid structure that is periodic in all directions.

Care must be taken in selecting the amount of water to be added in the z direction. Adding too little water might cause the simulation to become unstable or be unable to hold temperature. With too little water on each side of the pore there is also the unique problem that each side of the membrane is closer to the image of the other side than the thickness of the membrane. This can cause strange effects if looking at ionic current through the pore or capacitance. Adding too much water merely causes the simulation to run slowly because of the increased number of atoms to simulate. Thus it is generally safer to add too much water than too little. In the studies represented in this dissertation, there was a water cushion of 6 to 10 nm.

After adding water, the ions can be added to the system. The autoionize plugin is called from a script to add sodium and chloride ions to the solution. This is a process where a water molecule is picked at random from a list, and if it is not too near an ion, it is replaced by an ion. This is then repeated until the desired Molarity is achieved. At this step, the net charge of the system is brought to zero as well. For example if there is DNA in the simulation box with a net charge of $-10e$, 10 more sodium ions than chloride ions are added. Once all of the sodium and chloride ions are added, the sodium ions can be replaced by potassium ions to more closely follow experimental technique.

3.2.4 Running the Simulation

The actual simulation is then started. The first step in the simulation is to minimize the static energy of the system. This is required so that the integration

does not destabilize at the initial frame of the simulation due to large forces. Once each of the atoms is affected by a net force that is below a certain threshold the minimization is complete.

After the energy minimization, the atoms have a velocity of zero assigned to each of them. Thus their total energy (potential + kinetic) is very small, corresponding to a very low temperature. Experiments with nanopores are generally done near room temperature, so the system must be brought up to 295K. This is done by assigning a random velocity to each atom consistent with a specified temperature. To avoid problems with suddenly assigning a large velocity to all of the atoms in the simulation, the temperature is slowly ramped up from 0K all the way up to 295K, reassigning random velocities from the proper distribution every timestep.

The next step after bringing the temperature up is to set the pressure. When the water was added to the system, the number of water molecules needed to achieve a realistic result was guessed. Now the simulation box must be altered to fine-tune the pressure given the fixed number of water molecules present. A Nosé-Hoover Langevin piston is used to control the pressure, with a temperature target of 295K. Also, the temperature of the system is held steady using Langevin dynamics with the same temperature target, so that the simulation is running in the NPT ensemble. Because the silicon-nitride is periodic in the x-y plane, the cell cannot shift much in those directions, therefore the cell must elongate or shrink in the z direction to arrive at the correct pressure. By looking at the volume of the cell over time, the system can be seen settling to an equilibrium volume. Once this is done, the production simulation can begin.

The production simulation can now be run without the pressure barostat. The temperature is held constant with a Langevin dynamics damping term, and the volume is constant as well, which means the system is running in the NVT ensemble. If there is a silicon-nitride membrane present, the Langevin term is only applied to the silicon and nitrogen atoms. This allows the water and ions to be free from the direct forces that the Langevin dynamics adds, but still stabilizes the temperature by allowing the water molecules to thermalize with the pore material.

For some simulations, an electric field is explicitly added to the force field. The field is applied globally using the equation

$$\mathbf{F_i} = q_i \mathbf{E}$$

where $\mathbf{F_i}$ is the force on the ith atom, q_i is the charge on the ith atom, and $\mathbf{E}$ is the electric field applied to the simulation. This closely approximates the experimental method of setting up a potential difference between electrodes on either side of the pore. Water molecules are free to align with the field, so the electric field locally at any point in the simulation box will feel the effect of some fraction of the electric field applied. However, because the ions are free to move, they will counter the electric field in the bulk by building up charge on either side of the pore effectively creating a capacitor across the pore. This causes the potential to be approximately constant in the bulk water, and the majority of the potential drop to be across the pore.

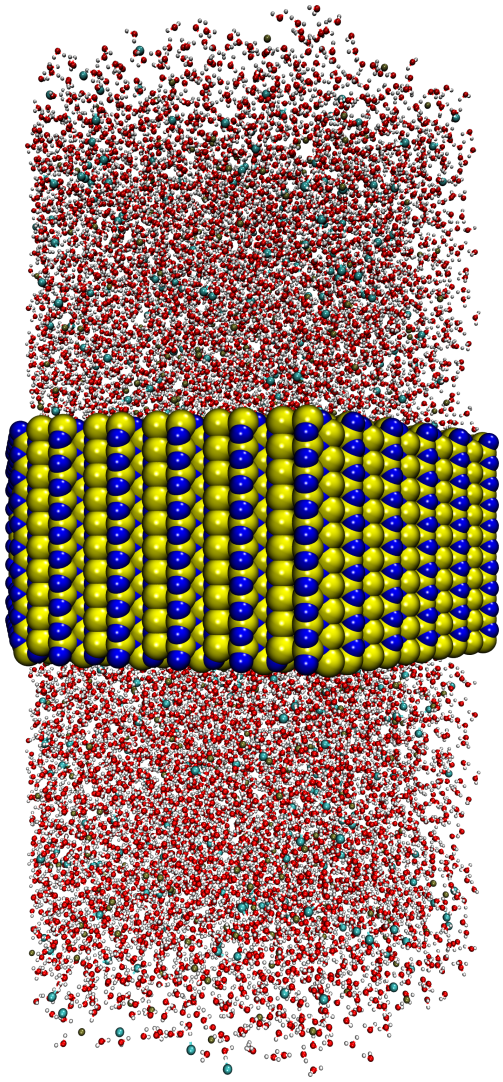

Figure 3.6: Side view of the membrane-pore-water-ion system. This pore is approximately 30Å thick, with 50Å of water on each side. This is a larger amount of water than needed to simply stabilize the system because the ionic current will be measured directly from the ion motion. It is more important to add water to act as "reservoirs" in this situation.

Chapter 4

Microcanonical Formalism

The preceding sections have endeavored to highlight methods of calculating *ionic* currents in nanoscale devices. It is equally important to expand upon methods of calculating *electronic* currents in nanoscale devices. For instance, it was necessary to calculate the electronic tunneling current between two electrodes in a pore to estimate the feasibility of discriminating DNA bases using transverse electronic transport [11, 12]. In those works, a tight-binding model was used to calculate the electronic structure, and then a Green's function approach was used to calculate the current through the system. This method is an example of using the Landauer-Buttiker formalism, where electrons are assumed to travel through a lead from a reservoir infinitely far away. The electrons are then scattered by the structure under study (in this example, water and DNA). Then transmittance data resulting from this calculation can be used to calculate the conductance of the system.

This approach to calculating the current worked well for Refs. [11, 12] because only relative currents were needed to be measured, the connections to the leads were assumed to be in linear response, and no dynamic information was needed from the system. If dynamical information is required from the calculation, Landauer formalism is unable to provide any help, as it is a strictly steady-state theory.

Another method for calculating current in nanoscale systems is the microcanonical formalism [27, 28, 29]. In this method of calculating current, the entire

system is simulated with time-dependent quantum mechanics, and the simulation is completely isolated. In essence, this method is just simulating a completely closed quantum mechanical system and measuring the movement of the electrons to get the current. There are no external leads or reservoirs to attach to the system. As such, this formalism is especially well suited to cold atoms research and cases with small isolated systems.

The formalism can be described as follows: first, the system is divided into two parts; we will denote them as left and right. A potential difference is imposed by hand between the two sides. One such method of providing that potential difference is to add a potential to the right side and calculate the ground state of the entire system. The Hamiltonian of the system would be constructed as follows:

$$H = \begin{cases} H_0 & \text{if } x \leq 0 \\ H_0 + V & \text{if } x > 0 \end{cases} \tag{4.1}$$

where H_0 is the unperturbed Hamiltonian, and V is a constant equal to the potential difference in the system that is being simulated. This will leave a greater density of electrons in the left half of the system.

After the ground state is calculated, the system is evolved forward in time using H_0 as the Hamiltonian. Because of the greater electron density in the left half, the left half will be at a higher potential than the right half. The current is then calculated by

$$I = \frac{dQ}{dt}$$

where Q is the total charge contained in the right half of the system. We can use this equation because the system is closed, and thus the current must only travel within the system.

However, even when approximating systems that are not isolated, the microcanonical formalism can be a useful tool. Small clusters of metal atoms can act as tiny capacitors to hold charge and allow a discharge across the system of interest. Simulations of 1D chains of atoms using tight-binding and modestly sized electrodes, of tens to hundreds of atoms on either side of a quantum point contact

show adherence to the 1-channel conductance formula [28].

$$G_0 = \frac{2e^2}{h} \approx 77.48\mu S$$

Furthermore, 3D simulations employing Time-Dependent Density Functional Theory (TDDFT) have similarly recovered the quantum of conductance above.[28]

This leads to the promise of being able to calculate currents in nanopore-sized systems using the microcanonical formalism, which would allow insight into the current dynamics of the system. One drawback of this microcanonical formalism is that it can only approximate a larger system for a very short amount of (simulated) time. Once the time dependent simulation of the system begins, there is a short time in which the system approaches a quasi steady-state [28]. During this time, the electrons transition from a non-current carrying state to a current carrying state. After this brief time, the system settles into a current carrying quasi steady-state. It remains in this state until the breakdown time τ_{BD} at which time the current drastically drops and becomes negative. This breakdown time is the time that it takes the fastest moving electrons to move from the center of the system (where the current is being measured) to the boundary and back again. This means that τ_{BD} scales linearly with the system size.

4.1 Stochastic Schrodinger Equation

One of the difficulties of using the microcanonical formalism to calculate current dynamics in nanoscale systems is the short amount of time in which the system is in a quasi steady state. This time may be lengthened by increasing the size of the electrodes in the simulation, but quantum mechanical simulation methods grow at order N^3 or greater, while the breakdown time only grows at order N. Clearly, the system cannot be run to an arbitrary length of time with these scaling rates even with very fast computers.

Chapter 7 of this dissertation outlines a method to extend the time in which the system is in a quasi steady state. The method mimics the effect that a battery would have on a system, and it does this by employing an open quantum systems

approach to the problem. Much of quantum mechanics is practiced assuming a closed system that does not receive energy or particles from outside. The simulation is in effect performed in a vacuum. Open quantum systems, however, simulate effects from interactions with the environment. The environment may add or take away energy, or even particles from the system.

One method of simulating the environment's effect on a system is using the stochastic Schrodinger equation shown below (SSE)[30, 31].

$$d\Psi = \left[-i\hat{\mathbf{H}}\Psi - \frac{1}{2}\hat{\mathbf{S}}^{\dagger}\hat{\mathbf{S}}\Psi\right]dt + \hat{\mathbf{S}}\Psi dW \tag{4.2}$$

where $\hat{\mathbf{H}}$ is the Hamiltonian of the system without interactions with the environment, S is a bath operator, and W is a Wiener process such that $\overline{dW} = 0$, and $\overline{dW^{\dagger}dW} = dt$.

It can be helpful to think of the stochastic portion of the SSE as providing "kicks" from the environment. It must be noted that these "kicks" are not energy conserving, and may add or take away energy from the system. Chapter 7 uses this formalism to describe a method of simulating a battery where the SSE "kicks" the system into a current-carrying state, and in essence recharges it so that the system can stay in a quasi steady state indefinitely. This in turn could be a useful tool to model current dynamics in nanoscale devices.

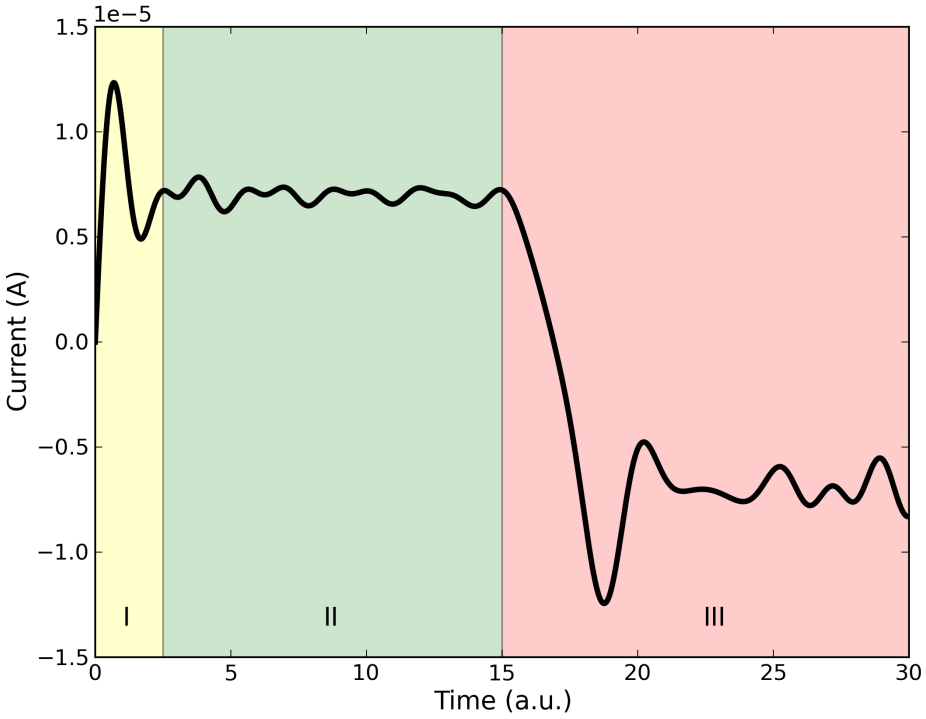

Figure 4.1: Current in a 1D system consisting of $N = 32$ sites simulated with a tight binding model. The current is measured in the center of the system by measuring dq/dt of the left half. The graph is divided into three sections, with the first section (yellow) being the transient initial phase. The second section (green) is the quasi steady state phase, and the third section (red) is the breakdown phase. Phase I shows the transition from a non-current-carrying state into a current-carrying state. Phase II approximates the current of a larger system containing leads and a battery. Phase III starts when the highest energy electrons "feel" the edge of the system and return to the middle.

Chapter 5

Dehydration and ionic conductance quantization in nanopores

5.1 Introduction

The behavior of water and ions confined in nanoscale geometries is of tremendous scientific interest. On the one hand, biological ion channels, which form from membrane proteins, perform crucial functions in the cell [47, 48]. On the other hand, there have been recent advances in aqueous nanotechnology such as nanopores and nanochannels, which hold great promise as the basic building blocks of molecular sensors, ultra-fast DNA sequencers, and probes of physical processes at the nanoscale [46]. Indeed, nanopore-based proposals for DNA sequencing range from measuring transverse electronic currents driven across DNA [12, 11, 49, 50, 51] to voltage fluctuations of a capacitor [52, 53, 54] to ionic currents [6, 55, 56, 57, 36, 58, 59, 60].

Recent experiments show that we are tantalizingly close to realizing a device capable of ultra-fast, single-molecule DNA sequencing with nanopores: identification of individual nucleotides using transverse electronic transport [61, 62] has been demonstrated. Discrimination of nucleotides using their ionic blockade cur-

rent when driving them individually though a modified biological pore has also been demonstrated [63, 64]. In these systems, the presence of water and ions will affect the signals and noise measured and thus understanding their behavior is an important issue in both science and technology.

Many computational studies have been dedicated to relating the three-dimensional structure [65, 47, 66] of biological ion channels to their physiological function, e.g., ion selectivity. For instance, recent studies have examined the role of ligand coordination in potassium selective ion channels [67, 68, 69, 70]. Biological channels, however, are complex pores with many potential factors contributing to their operation. Thus, only in a limited number of cases have universal mechanisms of ion transport been investigated, such as the recent work on the role of "topological constraints" in ligand coordination [71, 72, 73].

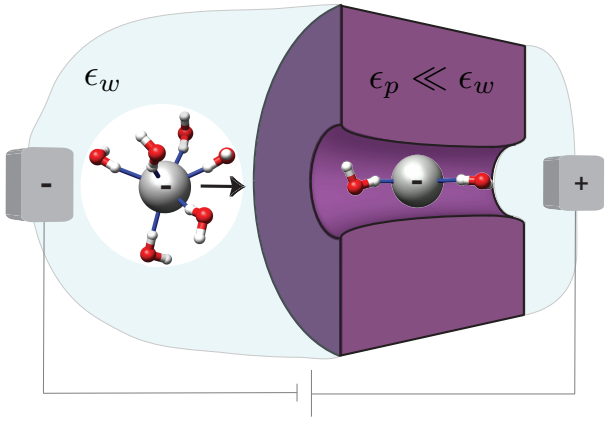

Figure 5.1: Schematic of ion transport in the presence of hydration layers. Only the first hydration layer is shown for simplicity. Ions in bulk water form hydration layers that make the ion behave as a "quasi-particle" that includes the ion and tightly bound water molecules. This quasi-particle is then solvated in the high-dielectric water. As the ion goes from the bulk solution to the pore it has to partially shed its hydration layers, i.e., the quasi-particle has to break apart. This gives a nonlinearity in the energetic barrier to transport. A continuum picture neglects these features and considers only the dielectric barrier that ions have to overcome by moving from bulk water with dielectric constant ϵ_w into the inhomogeneous, low-dielectric pore environment with $\epsilon_p \ll \epsilon_w$. Specialized proteins facilitate this process in biological ion channels via the presence of localized surface charges/dipoles and other mechanisms.

Fundamental developments in the fabrication of synthetic nanopores [74,

75, 16, 76, 77, 78, 79, 80], however, open new venues for investigating the behavior of ion channels and dynamical phenomena of ions, (bio-)molecules, and water at the nanoscale. For instance, what are the dominant mechanisms determining ionic currents and selectivity? What role do binding sites play versus hydration in constrained geometries? How accurate are "equilibrium" and/or continuum theories of ion transport? Well-controlled synthetic pores can be used in this context to examine how ion transport is affected, for instance, by changing only the pore radius, in the absence of binding sites and significant surface charge within the pore.

In this paper we examine the role of dehydration in ionic transport through nanopores. In particular, we investigate the recent prediction of quantized ionic conductance by two of the present authors (MZ and MD) [81], namely that drops in the conductance, as a function of the effective pore radius, should occur when successive hydration layers are prevented from entering the pore. This effect is a classical counterpart of the electronic quantized conductance one observes in quantum point contacts as a function of their cross section (see, e.g., Ref. [82]). We examine different ions, both positive and negative, and of different valency (namely, Cl^-, Na^+, K^+, Ca^{2+}, and Mg^{2+}). We find that the ion type plays only a minor role in the radii of the hydration layers, and thus does not affect much the pore radii at which a sudden drop in the current is expected. Divalent ions, however, are the most ideal experimental candidates for observing quantized ionic conductance because of their more strongly bound hydration layers. Further, the fluctuating hydration layer structure and changing contents of the pore should give a peak (versus the effective pore radius) in the relative current noise - giving an additional method to observe the effect of the hydration layers. Thus, we elucidate how quantized ionic conductance provides a novel tool to deconstruct the energetic contributions to ion transport.

The paper is organized as follows: In Sec. 5.2, we give a macroscopic (i.e., a continuum electrostatic) viewpoint on the energetics of ion transport. In Sec. 5.3, we examine how ions induce local structures in the surrounding water known as hydration layers - an effect that is not taken into account when using continuum

electrostatics to estimate energetic barriers to transport. Further, we calculate the energies stored in these layers and develop a model for the energetic barrier for ions entering a pore. In Sec. 5.4, we use a Nernst-Planck approach to relate this barrier to the ionic current. In Sec. 5.5, we discuss how the presence of the hydration layers gives rise to a peak in the relative noise in the ionic current at values of the effective pore radius congruent with a layer radius. In Sec. 5.6, we then present our conclusions.

5.2 Ionic Transport

The experimental set-up we are interested in is that of ions driven through a pore/channel of nanoscale dimensions under the action of a static electric field [1]. Such a situation is depicted in Fig. 5.1. A simple approach to ionic transport is to envision the ions moving through an energetic barrier due to going from the high-dielectric aqueous environment into the inhomogeneous, low-dielectric environment of the pore, treating the surroundings as continuum media. The resulting approach is inherently static: by analyzing the energetic barrier to (near-equilibrium) transport one obtains information about how different factors - the pore material (through its dielectric constant), the pore dimensions, the presence of surface charges, and the presence of the high-dielectric water along the pore axis - would affect transport.

Indeed, one of the first calculations of the dielectric barrier (using a "Born solvation" model) was done by considering the ion solvated in water and moved into a low-dielectric, pore-less membrane [83, 84]. This provides an estimate of the energies involved by calculating the energy change of solvating the ion in continuum water, with dielectric constant $\epsilon_w \approx 80$, to "solvating" it in a continuum material with $\epsilon_p \approx 2$ (representative of lipid membranes [2]). For instance, the energy change of a Cl^- ion, with effective radius $R \approx 2\,\text{Å}$ [3], moved from continuum water to the

[1] Although similar conclusions should apply in other scenarios such as the generation of a concentration gradient.

[2] In pores - especially biological pores - the membrane dielectric constant, ϵ_m, and the dielectric constant of the pore material, ϵ_p, can be different.

[3] The effective radius can be estimated from, e.g., molecular dynamics simulations that give

continuum material is

$$\Delta U = \frac{e^2}{8\pi R\epsilon_0}\left(\frac{1}{\epsilon_p}-\frac{1}{\epsilon_w}\right) \quad (5.1)$$

$$\approx 1.8\,\text{eV}. \quad (5.2)$$

This is quite a substantial energy change - about half the solvation free energy of Cl^- [47, 87]. The finite thickness of the membrane does not change this value significantly. For thick membranes, it is lowered by [83, 84]

$$\frac{e^2}{4\pi\epsilon_0\epsilon_p l}\ln\left(\frac{2\epsilon_w}{\epsilon_w+\epsilon_p}\right),$$

for $\epsilon_w \gg \epsilon_p$, where l is the membrane thickness (and pore length). For $\epsilon_p \approx 2$ and $\epsilon_w \approx 80$, this gives $\sim 5/l\,\text{eV}\,\text{Å} \approx 0.1\,\text{eV}$ for a membrane of thickness $l = 50\,\text{Å}$. That is, the Born estimate in Eq. (5.1) is lowered to $\sim 1.7\,\text{eV}$. Obviously, the membrane width [88] and composition can play a significant role in this estimate. For the common synthetic pores made of silicon dioxide ($\epsilon_p \approx 4$) or silicon nitride ($\epsilon_p \approx 7.5$) the estimate in Eq. (5.1) is reduced from $\sim 1.8\,\text{eV}$ to $\sim 0.9\,\text{eV}$ and $\sim 0.4\,\text{eV}$, respectively. These barriers are more than an order of magnitude larger than k_BT at room temperature, where k_B is the Boltzmann constant.

Due to this magnitude, it is clear that the energy scale of solvation is one of the controlling factors in ion transport. However, in addition to the above there is water present in the pore. One expects, therefore, that the energy of solvation would be decreased from simple estimates like that of Eq. (5.1). Several groups have calculated this contribution [83, 84, 88, 89, 90]. For instance, Ref. [91] shows that the energy barrier of bringing an ion from continuum water into a low-dielectric, continuum membrane is reduced from $\sim 40\,\text{kcal/mol} \approx 1.7\,\text{eV}$ to $\sim 20\,\text{kcal/mol} \approx 0.9\,\text{eV}$ by the presence of water in the pore. This demonstrates that a pore filled with a high dielectric medium (e.g., continuum water) can significantly lower the barrier to transport. Even still, the barrier remains substantial.

In biological systems, however, the pores provide a channel with a much lower barrier as indicated by the conductance of many biological ion channels.

a surface where the screening charge due to the hydrogen or oxygen atoms of water fluctuates. For instance, Figs. 5.2 and 5.3 show this surface (see also Refs. [85, 86]).

These pores are formed from specialized proteins whose role is precisely to facilitate passage of ions (and further to selectively allow passage of certain ions). Clearly, pores with internal charges and/or dipoles can significantly reduce the energetic barriers for transport. Indeed, the effect of surface charges has been calculated in clean pores [92, 93, 94] and when present in sufficient amounts would negate the effect we predict as the reduction of the energetic barrier would be comparable to, or larger than, the hydration layer energies. Therefore, our interest is in clean pores with little to no surface charge where clear-cut experiments can be performed to understand the effect of hydration on transport. This rules out the direct use of some biological ion channels, particularly those with very small pores where single-file transport occurs [95, 65, 96], because of the presence of localized charges and dipoles.

To conclude this section, we note that the continuum description suffers from a number of issues at the nanoscale: it is only valid beyond the correlation length of the material [97], which for the strong fields around an ion is $\sim 8\,\text{Å}$ for water (see below), similar to the $\sim 5-8\,\text{Å}$ in water only [98]; linear continuum electrostatics is only valid when the polarization field is co-linear with the electric field (not the case in the hydration layers we discuss below); in a related issue, it is only valid for weak fields (in the context of ion channels, see, for example, Sec. 3.4 in Ref. [91]); there is also an issue of where the "surface" separating the charge and the dielectric membrane/continuum water is located, especially for fluctuating atomic ensembles as is the case for protein pores and molecular (rather than continuum) water. Thus, while a continuum picture can highlight some general features of the energetic barrier to ion transport - in some cases giving compact analytical expressions - it breaks down when trying to understand the effect of structure at the nanoscale. In fact, macroscopic, continuum electrostatics is not designed to study specific features or short-range interactions at these length scales. This is precisely what we seek to address in the following sections.

5.3 Hydration of Ions

We begin our study of quantized conductance by first illustrating how ions are hydrated in solution and then discuss the energies involved in this process. The formation of hydration layers around ions has been known for some time (see, e.g., Ref. [47]), and is due to the strong local electric field around the ion and to repulsive short-range interactions among molecular/atomic species. We use molecular dynamics (NAMD2 [19]) simulations to understand the structure of hydration layers when different ions are inside and outside of nanopores [4].

Figures 5.2 and 5.3 show the water density oscillations for several common ionic species [5]. There is a strong peak in water density about 3 Å away from the ions, with two further oscillations after that spaced about 2 Å apart. These oscillations signify that there are strongly bound water molecules forming around the ions. Table 5.1 lists the hydration layer radii from both this study and experiment. We find very good agreement with the experimental data for all cases. The water density approaches the bulk value ($\sim 0.033\,\mathrm{Molecules/\AA^3}$) at about 10 Å, which is also consistent with the experimental value.

The oscillations in water density also give rise to oscillations in the local electric field. Figures 5.2 and 5.3 show this for monovalent and divalent ions where the time-averaged electric field was calculated from the bare ion value plus a sum over all partial charges given by the hydrogen and oxygen atoms of water [6]. In the

[4]For an ion in bulk water, we simulated a hexagonal box of 150 Å height and 43 Å radius with periodic boundary conditions in all directions. We then fixed an ion in the center of the box and counterion(s) near the edge of the box, far away from the ion of interest. For an ion in a pore, a cylindrical pore of radius R was cut into a hexagonal silicon nitride film 97 Å thick and of 29Å radius. This was accomplished by removing all silicon and nitrogen atoms within a distance R from the z-axis. An ion was fixed in the middle of the pore and counterion(s) were fixed outside of the pore. The system was then solvated in water resulting in a box of linear dimension 167 Å in the z-direction. An energy minimization procedure was then run, the system was heated up to 295 K, and finally the production run started. The first 600 ps were discarded to remove artifacts from the initial conditions and the information from the subsequent 2 ns collected. Other simulation details are as in Ref. [51].

[5]We calculated the density of water surrounding each ion by placing $1\,\mathrm{\AA^3}$ shells concentric with the ion. The inner shells have a larger width to give the same volume. We then counted the number of atoms (either hydrogen or oxygen) within each of the shells throughout the 2 ns simulation at time intervals of 200 fs. Due to the smaller bin sizes, the plots have minor differences from Ref. [81] at small distances from the ion.

[6]The electric field was calculated by summing the contributions from the ion and all partial

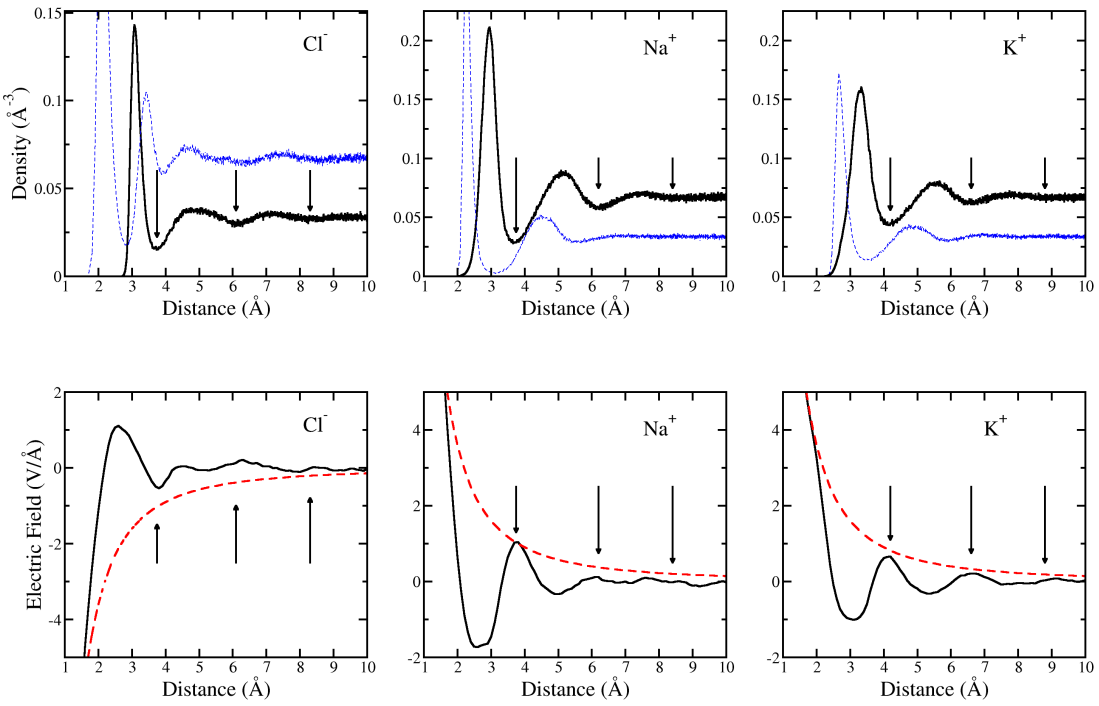

Figure 5.2: Top panels: Water density oscillations versus distance for Cl^-, Na^+, and K^+ in bulk water. Black, solid lines indicate the density calculated from the oxygen atom positions for Cl^- and hydrogen atom positions for the cations. The arrows indicate the minimum in the density oscillations. The blue, dashed lines indicate the density calculated from the hydrogen atom positions for Cl^- and oxygen atom positions for the cations. Bottom panels: The electric field due to both the bare ion (red, dashed line) and due to the ion plus partial charges on the water molecules (black, solid). The arrows again indicate the minimum in the density oscillations.

figures, the first hydration layer gives pronounced field oscillations for all species examined. The other oscillations in the field are more well-defined for K^+, Ca^{2+}, Mg^{2+}, and to some extent Na^+, compared to Cl^-. Anions, such as Cl^-, have a different structure of the water around them compared to cations: in the first layer, they pull one of the hydrogen atoms of each of the water molecules closer while the other interferes with the formation of the second layer, possibly hindering the

charges (on the hydrogen and oxygen of the water) within 15 Å from every field point. The angular component to the field was several orders of magnitude smaller because the time-averaged field has essentially spherical symmetry. In Ref. [81] all water molecules were modeled as dipoles.

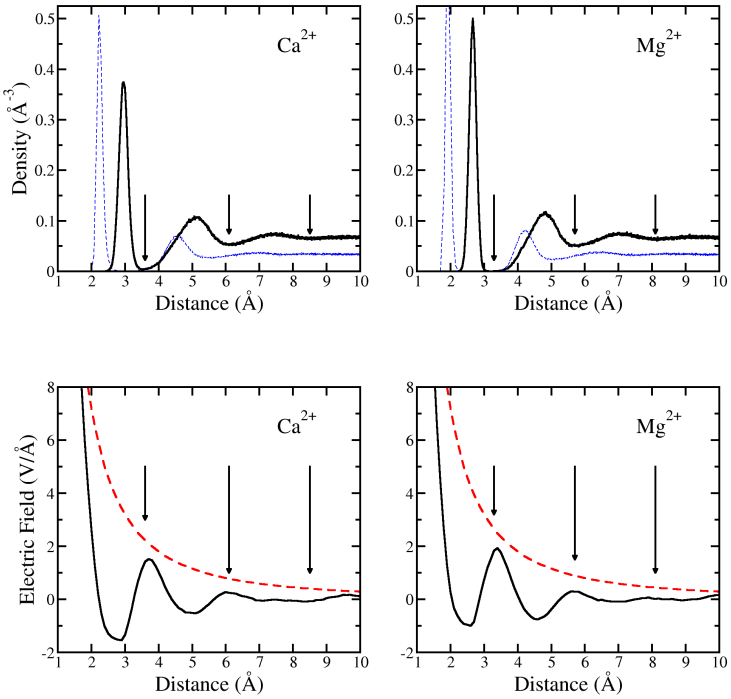

Figure 5.3: Top panels: Water density oscillations versus distance for Ca^{2+} and Mg^{2+} in bulk water. Black, solid lines indicate the density calculated from the hydrogen atom positions. The arrows indicate the minimum in the density oscillations. The blue, dashed lines indicate the density calculated from the oxygen atom positions. Bottom panels: The electric field due to both the bare ion (red, dashed line) and due to the ion plus partial charges on the water molecules (black, solid). The arrows again indicate the minimum in the density oscillations.

ability of the second layer to form a "perfect" screening surface. The fact that the electric field is not simply suppressed by $1/\epsilon_w$ shows the difficulty of a macroscopic (continuum) dielectric picture to predict behavior at the nanoscale (similar to well-known features in other systems such as Friedel oscillations and apparent from the derivation of continuum electrostatics, where averaging is required over length scales much larger than the correlation length of the material [97]).

We now estimate the energies contained in these layers, which we list in Table 5.1. The electric fields seen in Figs. 5.2 and 5.3 show an oscillating behavior that is reminiscent of a set of Gauss surfaces, i.e., layers of alternating charge that screen the field of the ion. Thus, in order to estimate the energies contained in the

Table 5.1: Table of physical quantities from simulation and experiment. The theoretical hydration layer radii, R_i, for all three layers are defined using the ion-oxygen distance for Cl^- and ion-hydrogen distance for the cations. The first oxygen density maximum, R_{XO}, is for all ions X using the present theory and experiment (average values taken from Ref. [99]). The second maximum is also shown for the divalent ions from both theory and experiment. The inner/outer radii that enter Eq. (5.3) are shown, the first of which is calculated such that Eq. (5.3) equals ΔG (exp) when $R_{i\nu}^O \to \infty$ (see also text). The next three inner/outer radii are taken from the minima of the oxygen density for Cl^- and the minima of the hydrogen density for the cations. Further, we report the layer energies U_i (using $\epsilon_p = 1$), and the Gibb's free energy from experiment [87], and the experimental mobilities [47] used in this work.

Ion	R_i (Å) (th)	R_{XO} (Å) (th)	R_{XO} (Å) (exp)	R_I, R_O (Å)	$-U_i$ (eV) (th)	$-\Delta G$ (eV) (exp)	μ (m^2V/s) (exp)
Cl^-	3.1, 4.9, 7.1	3.1	3.19	2.0, 3.9, 6.2, 8.5	1.73, 0.68, 0.31	3.54	7.92×10^{-8}
Na^+	2.9, 5.1, 7.5	2.3	2.44	1.9, 3.8, 6.2, 8.4	1.51, 0.72, 0.30	3.80	5.19×10^{-8}
K^+	3.3, 5.6, 7.8	2.7	2.81	2.4, 4.2, 6.6, 8.8	1.15, 0.61, 0.27	3.07	7.62×10^{-8}
Ca^{2+}	3.0, 5.1, 7.5	2.2, 4.6	2.42, 4.55	1.8, 3.6, 6.1, 8.5	7.89, 3.23, 1.32	15.65	6.17×10^{-8}
Mg^{2+}	2.7, 4.8, 7.1	1.9, 4.2	2.09, 4.20	1.5, 3.3, 5.7, 8.1	10.33, 3.62, 1.48	19.03	5.5×10^{-8}

layers, we replace the microscopic structure giving rise to the complex field by a set of surfaces as shown in Fig. 5.4 that perfectly screen (with dielectric constant ϵ_w), rather than over-screen, the ion charge.

Within this picture, the energy of the i^{th} hydration layer of ionic species ν is [81]

$$U_{i\nu}^o = \frac{q_\nu^2}{8\pi\epsilon_0}\left(\frac{1}{\epsilon_p} - \frac{1}{\epsilon_w}\right)\left(\frac{1}{R_{i\nu}^O} - \frac{1}{R_{i\nu}^I}\right), \tag{5.3}$$

where q_ν is the ionic charge and $R_{i\nu}^{I\,(O)}$ are the inner (outer) radii demarcating the hydration layer as obtained from the water density oscillations. In order to obtain the innermost radius we compute the total solvation energy, $U_T = -q_\nu^2\left(\epsilon_w - \epsilon_p\right) / \left(8\pi\epsilon_0\epsilon_p\epsilon_w R_{1\nu}^I\right)$, and compare with the experimental free energies [87], which are dominated by the electrostatic energy. These free energies, together with the layer energies (for $\epsilon_p = 1$), are tabulated in Table 5.1. Except for the third hydration layer for monovalent ions, the layer energies are greater than other free energy contributions such as the entropy change due to the water structure or van der Waals interactions [100, 101]. In Eq. (5.3) we have also added a possible screening contribution, ϵ_p, from the pore material and/or charges on the surface of the pore. In Ref. [81] this was assumed to be one: the low-dielectric pores reduce the energy barrier only by a small amount and in a different func-

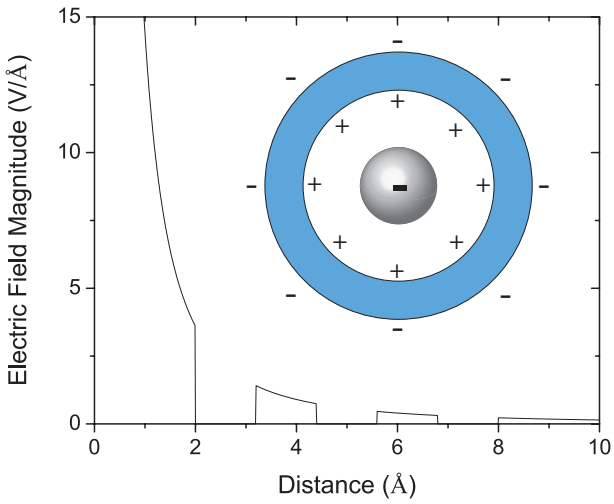

Figure 5.4: The magnitude of the approximate electric field (given by a set of Gauss surfaces, see inset) used to represent the fields in Figs. 5.2 and 5.3, and also used to calculate the energy contained in each layer (Eq. (5.3)).

tional form. In Sec. 5.5 we will discuss the effect of this screening on the detection of quantization steps.

Previously, we proposed a model for how the energy is depleted in a hydration layer as the effective radius of the pore, R_p, is reduced [81]. In this model, the energy change is proportional to the remaining surface area of a hydration layer within a pore. It takes into account both that the water-ion interaction energy of small water clusters is approximately linear in the number of waters [101, 102] and that molecular dynamics simulations show a time-averaged water density with partial spherical shells when an ion is inside a pore of small enough radius (see Fig. 1 in Ref. [81]). Contributions from, e.g., van der Waals interactions with the pore and changes in the water-water interaction, are small [100, 101]. Thus, the energy of the remaining fraction $f_{i\nu}$ of the i^{th} layer in the pore is taken as $U_{i\nu} = f_{i\nu}U^o_{i\nu}$. The fraction of the layer intact is $f_{i\nu} = S_{i\nu}/4\pi R^2_{i\nu}$ where $S_{i\nu}$ is the surface area (of the spherical layer) remaining where the water dipoles can fluctuate. The latter is given by

$$S_{i\nu} = 2\Theta\left(R_{i\nu} - R_p\right)\int_0^{2\pi} d\phi \int_0^{\theta_{c\nu}} d\theta R^2_{i\nu}\sin\theta, \tag{5.4}$$

where $\Theta\left(x\right)$ is the step function and $\theta_{c\nu} = \sin^{-1}(R_p/R_{i\nu})$. When $R_p < R_{i\nu}$, the

fraction of the surface left is

$$f_{i\nu}\left(R_p\right) = 1 - \sqrt{1 - \left(\frac{R_p}{R_{i\nu}}\right)^2}. \tag{5.5}$$

The total internal energy change will then result from summing this fractional contribution over the layers to get

$$\Delta U_\nu(R_p) = \sum_i (f_{i\nu}(R_p) - 1) U^o_{i\nu}. \tag{5.6}$$

We stress first that the effective radius R_p is not necessarily the nominal radius defined by the pore atoms. Rather, it is the one that forces the hydration layer to be partially broken because it can not fit within the pore, and it could be smaller than the nominal pore radius by the presence of, e.g., a layer of tightly bound water molecules on the interior surface of the pore. Second, our model misses internal features of the hydration layers themselves. For instance, Ref. [103] examines the first hydration layer structure in carbon nanotubes of different radii. These authors find a large increase in the energy barrier when the pore radius nears the inner hydration layer. They also seem to observe *sub-steps* in the water coordination number within the inner shell as the pore radius is reduced. Thus, although our model contains only a single "smoother" step, experiments could very well observe these internal sub-steps corresponding to the sudden loss of a single or few water molecules out of a given hydration layer.

Another basic assumption in our model is that the interaction energy of the water molecules in each layer is the same regardless of whether the ion is inside or outside of the pore. Figure 5.5 shows the distribution of the dipole orientation of water molecules both in bulk and inside pores of different radius [7]. The average dipole orientation of the waters changes very little inside the pore, as do their fluctuations, thus supporting this assumption.

[7] For each time step, all water molecules within a cylindrical annulus coaxial with the $+z$-axis were taken, where the annulus has a 1.5 Å width, 1.5 Å height, and a central ring 5 Å from the ion. Then the unit vector connecting the oxygen atom of those molecules to the midpoint between the hydrogen atoms (the unit dipole $\hat{\mathbf{p}}(t)$) was generated together with the unit position vector of the water molecules at the centroid of the molecule $\hat{\mathbf{r}}(t)$. We then took the scalar product $\hat{\mathbf{p}} \cdot \hat{\mathbf{r}}$ per molecule, and averaged over the molecules. This set of data was then made into a histogram of 501 bins evenly spaced from -1 to 1.

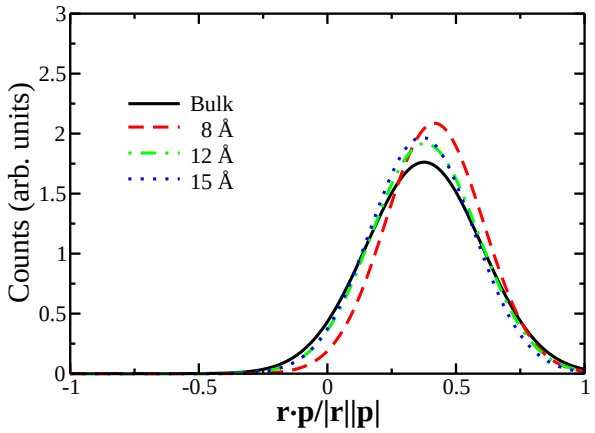

Figure 5.5: Distributions of the dipole orientations of water molecules within a cylindrical annulus 5 Å away from a Ca^{2+} ion in bulk (black line) and inside pores of radius 8 Å (red dashed line), 12 Å (green dash-dotted line) and 15 Å (blue dotted line). The mean value is around 0.38 (corresponding to the water dipole pointing 68 degrees away from the ion-water vector), except for the 8 Å pore, which increases to 0.42 (corresponding to the water dipole pointing 65 degrees away from the ion-water vector). This signifies a moderate tightening of the water dipole around the field of the ion as the pore size is reduced.

In order to make a connection with the ionic current (in Sec. 5.4 below), we calculate the free energy [8] change for species ν as

$$\Delta F_\nu = \Delta U_\nu - T\Delta S_\nu, \tag{5.7}$$

which includes an entropic contribution from removing a single ion from solution and localizing it in the pore region. This entropic contribution is $\Delta S_\nu = k_B \ln(V_p n_0)$, where we have assumed an ideal ionic solution and V_p is the volume of the pore and n_0 is the bulk salt concentration for all species ν. The free energy change is plotted in Figs. 5.6 and 5.7 versus the effective pore radius and it is substantial when the latter becomes smaller than the outer hydration layer.

[8] Here we deal with constant volume and temperature and thus use the Helmholtz free energy.

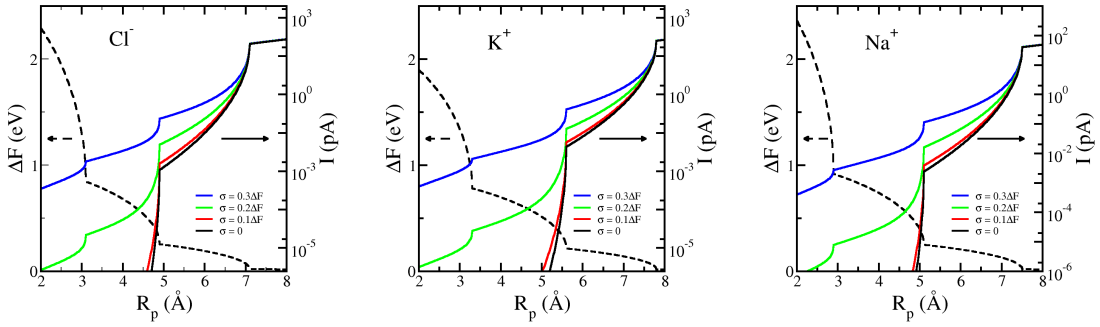

Figure 5.6: Free energy changes, ΔF_ν, and currents versus the effective pore radius for the monovalent ions and a field of $1\,\mathrm{mV/Å}$. The black, dashed line indicates the free energy change. The remaining lines indicate the current with different standard deviations of the noise (see text for details). The currents are for $\sigma = p\Delta F$, with $p = 0.3,\ 0.2,\ 0.1,\ 0$ from top to bottom.

5.4 Ionic Currents

We now want to relate these energy barriers to the ionic current through the pore [9]. We do this by solving the Nernst-Planck equation in one dimension. Since this model consistently solves for both drift and diffusion contributions to ionic transport, and yields a compact analytical expression, we use it below with the energetic barriers found from the above model of dehydration. Even though this analytical model does not include some effects such as ion-ion interaction, we expect that it is qualitatively accurate as discussed along with its derivation.

The steady-state Nernst-Planck equation (see, e.g., [104, 105, 47]) for species ν in one dimension (assuming variability on the pore cross-section is not important) is

$$J_\nu = -q_\nu D_\nu \left[\frac{dn_\nu(z)}{dz} + \frac{q_\nu}{k_B T} n_\nu(z) \frac{d\Phi_\nu(z)}{dz} \right], \tag{5.8}$$

[9] The most detailed information regarding ion channels and physical processes in nanopores is provided by Molecular Dynamics (MD) - but MD simulations are not able to reach the necessary time scales required to extract the full information on the current. Indeed, there is a hierarchy of approaches going down from macroscopic to microscopic models: continuum models - Poisson-Boltzmann, Poisson-Nernst-Planck; Brownian dynamics; classical then quantum Molecular Dynamics. In practice, some combination of the different approaches is often used, such as calculating structural/energetic properties from MD and using them to construct simpler model systems that can then be tested experimentally. This is the approach we have followed in this work.

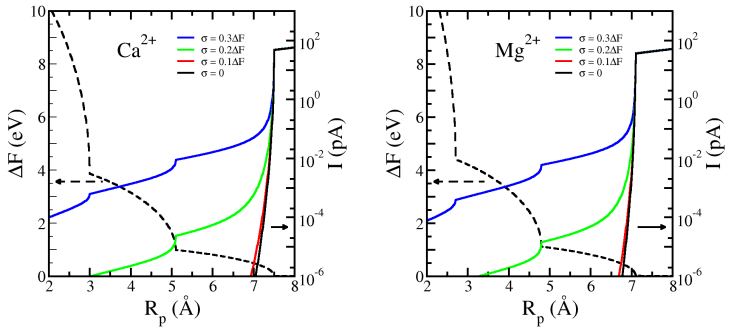

Figure 5.7: Free energy changes, ΔF_ν, and currents versus the effective pore radius for the divalent ions and a field of 1 mV/Å. The black, dashed line indicates the free energy change. The remaining lines indicate the current with different standard deviations of the noise (see text for details). The currents are for $\sigma = p\Delta F$, with $p = 0.3$, 0.2, 0.1, 0 from top to bottom.

where J_ν is the charge flux for species ν, $z \in (0, l)$ is the axial coordinate along the pore axis of length l, $n_\nu(z)$ is the ion density, D_ν is the diffusion coefficient (assumed to be position independent), and $\Phi_\nu(z)$ is the position-dependent potential (including both electrostatic and other interactions that change the energy within the pore). A full solution would require solving the density and potential within the reservoirs and pore simultaneously (see, e.g., Ref. [106]). However, we deal with high-resistance pores. Thus, we approximate the left (L) and right (R) reservoirs with constant concentrations n_L and n_R, and the boundary conditions at the edge of the pore are $n_\nu(0) = n_L$ and $n_\nu(l) = n_R$. This is equivalent to assuming that as soon as an ion leaves or enters the pore, the ions in the immediate surroundings of the pore equilibrate rapidly to their prior distributions. Thus, multiplying by $\exp(q_\nu \Phi_\nu(z)/k_B T)$ to get

$$J_\nu e^{q_\nu \Phi_\nu(z)/k_B T} = -q_\nu D_\nu \frac{d}{dz}\left[n_\nu(z)\, e^{q_\nu \Phi_\nu(z)/k_B T}\right]$$

and integrating yields the flux for species ν as

$$J_\nu = -q_\nu D_\nu \frac{n_R e^{q_\nu \Phi_\nu(l)/k_B T} - n_L e^{q_\nu \Phi_\nu(0)/k_B T}}{\int_0^l dz e^{q_\nu \Phi_\nu(z)/k_B T}}.$$

We make the further simplifying assumption that the electrostatic potential drops linearly over the pore - recognizing that in the presence of a significant potential

barrier, e.g., due to the stripping of the water molecules from the hydration layers and in the absence of surface/fixed charges in the pore, the ionic density in the pore is small and thus the field is due to ionic charge layers on both sides of the pore. Results from many works that include ion-ion interactions indeed find a linear drop of the potential across the pore (see, e.g., Ref. [107]). In this case, ions form a capacitor across the pore and every so often one ion translocates through the pore. The "healing" time for the loss of this ion is very short [107] and, thus, the field (potential drop) is not strongly affected [10]. Also, we assume that the potential barrier due to changes in these other interactions is constant over the pore - this ignores a region near the pore entrance, but will not qualitatively change the solution. Therefore, the potential for species ν can be written as

$$\Phi_\nu(z) = z\frac{V}{l} + \frac{\Delta F_\nu}{q_\nu}$$

when $z \in (0, l)$. The boundaries are given by $\Phi_z(0) = 0$ and $\Phi_z(l) = V$. Performing the remaining integral and for equal reservoir densities (our case), $n_L = n_R = n_0$, we get

$$J_\nu = -\frac{q_\nu^2 n_0 D_\nu V}{l k_B T} e^{-\Delta F_\nu / k_B T}.$$

Relating the diffusion coefficient to the mobility via the Einstein relation, $\mu_\nu = q_\nu D_\nu / k_B T$, and putting in the constant electric field $E = V/l$, one obtains

$$J_\nu = -q_\nu n_0 \mu_\nu E e^{-\Delta F_\nu / k_B T}. \tag{5.9}$$

That is, the flux of an ionic species is proportional to the electric field and density, where the latter is suppressed by a Boltzmann factor [81].

Now that we have an expression relating the energy barrier to the transport properties, we can calculate the current as a function of effective pore radius by

[10] One may worry that these charge layers - which mainly are due to excess ionic density - invalidate the assumption of constant ionic density outside the pore. A quick estimate of the excess density comes from the surface charge (for two parallel plates) necessary to give a typical potential drop of 100 mV over 100 Å. This is $\sigma = \epsilon_0 V/l \approx 5.5 \times 10^{-6}\, e/\text{Å}^2$. This surface charge is likely contained in a layer ~ 10 Å thick, giving a density $5.5 \times 10^{-7}\, e/\text{Å}^3$. For comparison, at 1 M concentration the density is $6 \times 10^{-4}\, e/\text{Å}^3$ - that is, orders of magnitude larger than the variation in density necessary to give the electric field over the pore. However, increasing the bias or decreasing the bulk concentration or pore length may invalidate this assumption.

multiplying Eq. (5.9) by the area of the pore to get

$$\begin{aligned} I_\nu &= 2\pi R_p^2 J_\nu \\ &\equiv I_{\nu 0} e^{-\Delta F_\nu / k_B T}, \end{aligned} \tag{5.10}$$

where we have defined a standard current $I_{\nu 0} = -q_\nu n_0 2\pi R_p^2 \mu_\nu E$ that would flow in the absence of an energy barrier. The current (5.10), with the mobilities and energies in Table 5.1, along with Eqs. (5.3)-(5.7), is plotted in Figs. 5.6 and 5.7 as a function of effective pore radius and for a field of $1\,\mathrm{mV/Å}$ [11]. The energetic barriers create sudden drops when the pore radii are congruent with a hydration layer radius. These correspond to the quantized steps in the conductance.

5.5 Effect of noise

In a real experiment, there will also be fluctuations in the energetic barrier due to the fact that the hydration layers are not defined by their time-averaged value (i.e., they are not perfect spherical shells) and also due to fluctuations of the water structure and contents of the pore (both within a single experiment and also structural variations between experiments). Thus, we also examine the effect of these fluctuations and the current noise they induce. Thus, we calculate an averaged current for species ν as

$$\langle I_\nu \rangle = \langle I_{\nu 0} e^{-\Delta F_\nu / k_B T} \rangle. \tag{5.11}$$

We consider two specific models: Gaussian fluctuations of the free energy with a standard deviation proportional to the free energy barrier at a fixed pore radius and Gaussian fluctuations in the effective pore radius. The latter was also considered previously [81] where it was found that this type of noise smooths out the visibility of the drops in conductance (i.e., the peaks in the derivative $d\langle I_\nu \rangle / dR_p$ become smoother with increasing noise). However, it was also shown that this fluctuation

[11] We note that for all layers to be present, the applied field can not be stronger than the ion's field of $\sim 0.3\,\mathrm{V/Å}$ - the magnitude of a monovalent ion's field within the third layer (~ 7Å from the ion) - and approximately double that for divalent ions. In this way, the hydration layer structure will not be significantly perturbed.

induces a peak in the relative current noise that is much less sensitive to the strength of the fluctuations - thus giving an alternative method to detect the effect of the hydration layers. We develop a model for this relative noise here but do not perform the calculation of Eq. (5.11) for all the different species.

Fluctuating energy barrier - The first model we consider is an energy barrier that fluctuates according to a Gaussian distribution. We neglect fluctuations that make the barrier negative, so that the average current is

$$\langle I_\nu \rangle = \frac{I_{\nu 0}}{\mathcal{N}_\sigma} \int_0^\infty d\,(\Delta F)\; e^{-\Delta F/k_B T} e^{-(\Delta F - \Delta F_\nu)^2/2\sigma^2}, \tag{5.12}$$

where σ is the standard deviation of the fluctuations and

$$\mathcal{N}_\sigma = \int_0^\infty d\,(\Delta F)\, e^{-(\Delta F - \Delta F_\nu)^2/2\sigma^2}$$

is the normalization. The average current is thus

$$\langle I_\nu \rangle = I_{\nu 0} A e^{-\left(\Delta F_\nu - \sigma^2/2k_B T\right)/k_B T},$$

where the factor A is

$$A = \frac{\mathrm{erfc}\left[\left(-\Delta F_\nu + \sigma^2/k_B T\right)/\sqrt{2\sigma^2}\right]}{\mathrm{erfc}\left[-\Delta F_\nu/\sqrt{2\sigma^2}\right]}.$$

The value of A for small σ is very close to 1. Thus, the effect of a fluctuating energy barrier with small fluctuations is simply to lower the energy barrier by an amount $\sigma^2/2k_B T$. For stronger fluctuations, the factor containing the complementary error function, erfc, gives different limiting dependencies of the average current as the fluctuation strength σ is increased. However, large fluctuations are well outside the realm of validity of the present model.

The relative noise in the current provides even more information. The relative noise is

$$\Delta I_{\mathrm{rel}} = \frac{\sqrt{\langle I^2 \rangle - \langle I \rangle^2}}{\langle I \rangle}.$$

The expectation value of the square of the current is given by

$$\begin{aligned} \langle I_\nu^2 \rangle &= \frac{I_{\nu 0}}{\mathcal{N}_\sigma} \int_0^\infty d\,(\Delta F)\; e^{-\Delta F/k_B T} e^{-(\Delta F - \Delta F_\nu)^2/2\sigma^2} \\ &= B I_{\nu 0}^2 e^{-\left(2\Delta F_\nu - 2\sigma^2/k_B T\right)/k_B T}. \end{aligned} \tag{5.13}$$

Where the normalization is as before and the factor B is given by

$$B = \frac{\text{erfc}\left[\left(-\Delta F_\nu + 2\sigma^2/k_BT\right)/\sqrt{2\sigma^2}\right]}{\text{erfc}\left[-\Delta F_\nu/\sqrt{2\sigma^2}\right]}.$$

Thus, the relative current noise induced by an energy barrier with fluctuations is

$$\Delta I_{rel} = \sqrt{e^{\sigma^2/(k_BT)^2}\frac{B}{A^2} - 1}. \tag{5.14}$$

For small fluctuations, A and B depend very weakly on σ and are both very close to 1, giving a relative current noise

$$\Delta I_{rel} \approx \sigma/k_BT.$$

As expected, the relative noise increases with the strength of the fluctuations. For fluctuations proportional to the energy barrier, as shown in the Figs. 5.6 and 5.7, the fluctuations give rise to a monotonic increase in the relative noise. Overall, the effect of fluctuations in the energy barrier is to decrease the effective energy barrier and increase the current. This reduces the magnitude of the drops in the conductance but does not destroy their visibility. This would therefore help in observing quantized ionic conductance. It is worth noting, however, that this type of noise makes the step of the third hydration layer the most pronounced. This seems an unlikely situation in actual experiments and other types of noise need to be considered.

Fluctuating effective pore radius - In addition to the above noise, one expects that there would be fluctuations in the radii of the hydration layer/nanopore system. Previously, we demonstrated that this type of noise can smear the effect of the steps in the current [81]. As was seen, however, this noise also gives a peak in the relative noise in the current that is much less sensitive to the fluctuations than the average current. Here we develop a model of this behavior by calculating the relative noise assuming fluctuations across a single, perfect step in the free energy (see the inset of Fig. 5.8).

The average current due to species ν when averaged over fluctuations in the effective pore radius is

$$\langle I_\nu \rangle = \frac{1}{\mathcal{N}_\xi}\int_0^\infty dR\, I_{\nu 0}(R) e^{-\Delta F(R)/k_BT} e^{-(R-R_p)^2/2\xi^2}, \tag{5.15}$$

where ξ is the standard deviation of the radial fluctuations, $\mathcal{N}_\xi$ is the normalization, and the explicit R dependence has been included in both the barrier ΔF and the prefactor $I_{\nu 0}$. The dominant factor is the exponential of the free energy barrier and the quadratic dependence of $I_{\nu 0}$ on R can be ignored. For small fluctuations, the lower limit of the integral can be extended to $-\infty$ and $\mathcal{N}_\xi \to \sqrt{2\pi\xi^2}$ to give

$$\langle I_\nu \rangle = \frac{I_{\nu 0}(R_p)}{\sqrt{2\pi\xi^2}} \int_{-\infty}^{\infty} dR\, e^{-\Delta F(R)/k_B T} e^{-(R-R_p)^2/2\xi^2}. \tag{5.16}$$

Previously, we performed the averaging according to Eq. (5.15) [81], but here we instead use Eq. (5.16) with the approximate energy barrier $\Delta F\left(R\right) = \Delta F_h \Theta\left(R_h - R\right)$ of a single hydration layer of radius R_h and take $\bar{I}_{\nu 0}$ to be the current in the absence of the barrier. The average current then becomes

$$\langle I_\nu \rangle = \bar{I}_{\nu 0} \left[e^{-\Delta F_h/k_B T} \left(1 - C\right) + C \right],$$

where

$$C = \frac{1}{2} \mathrm{erfc} \left(\frac{R_h - R_p}{\sqrt{2}\xi} \right).$$

Similarly, for the square of the current one finds

$$\langle I_\nu^2 \rangle = \bar{I}_{\nu 0}^2 \left[e^{-2\Delta F_h/k_B T} \left(1 - C\right) + C \right].$$

Although $\langle I_\nu \rangle$ and $\langle I_\nu^2 \rangle$ are dependent on the strength of the fluctuations, ξ, the relative current noise has a universal behavior in the parameter $\tilde{R} = \left(R_h - R_p\right)/\sqrt{2}\xi$. That is, all features in the relative noise would be present regardless of the strength of the noise. However, the peak in the noise (see below) shifts to smaller values of R_p as the noise strength is increased, which is qualitatively in agreement with the full averaging (Eq. (5.15)) performed in Ref. [81].

The relative noise is

$$\Delta I_{\mathrm{rel}} = \frac{\sqrt{\left(1 - e^{-\Delta F_h/k_B T}\right)^2 C\left(1 - C\right)}}{e^{-\Delta F_h/k_B T}\left(1 - C\right) + C}.$$

For large or small R_p, the relative noise goes to zero, which can be seen from the properties of erfc that make $C \to 1$ and $C \to 0$ for large and small R_p, respectively. In between these limits, there would be nonzero relative noise, therefore indicating

that the relative noise would have a maximum. The peak in the relative noise occurs for $R_p < R_h$. For a large energy barrier ΔF_h, this peak occurs when C is small. Thus, we can approximate the relative noise as

$$\Delta I_{\rm rel} \approx \frac{\sqrt{C}}{e^{-\Delta F_h/k_BT} + C}.$$

This gives a peak in the noise when $C = e^{-\Delta F_h/k_BT}$ with a value

$$\Delta I^{\star}_{\rm rel} \approx \frac{1}{2} e^{\Delta F_h/2k_BT}. \tag{5.17}$$

The peak is exponentially large in the energy barrier. However, the model with the electrostatic energy given by Eq. (5.6) does not have an ideal step in the free energy (see, e.g., Figs. 5.6 and 5.7). From previous work [81], we can identify the peaks, $R_p^{\star}$, and use $\Delta F_h \approx \Delta F_\nu \left(R_p^{\star}\right)$. This is done in Fig. 5.8 for Cl^-. The model agrees quantitatively with the full averaging performed in Ref. [81]. The only feature missing is the additional background noise away from the step due to the non-uniform energy barrier on both sides of the step.

Thus, from this "two-channel" model of noise we have found two generic features: (*i*) a peak develops in the relative current noise that is exponentially high with the hydration energy barrier, and (*ii*) it is present regardless of the noise strength, although its location moves to smaller values of the pore radius with increasing noise (likewise, the peak becomes wider). These features are in agreement with what is found from performing the full averaging from Eq. (5.15) using the surface area model of the energy barrier [81]. In the full model the fluctuations will eventually smooth out the peak in the relative current noise. The latter, however, is still much less sensitive than the average current drops, making the peak in the relative current noise versus R_p a robust indicator of dehydration.

Barrier reduction - In addition to the above fluctuations, there are factors that reduce the energetic barrier, such as the presence of some surface charge and/or dielectric screening in the pore. In Eq. (5.3) we included a dielectric constant ϵ_p to represent a reduction in the hydration layer energy barrier from these sources. We expect, however, that the introduction of this constant overestimates the barrier reduction. It amounts to replacing the water molecules screening the

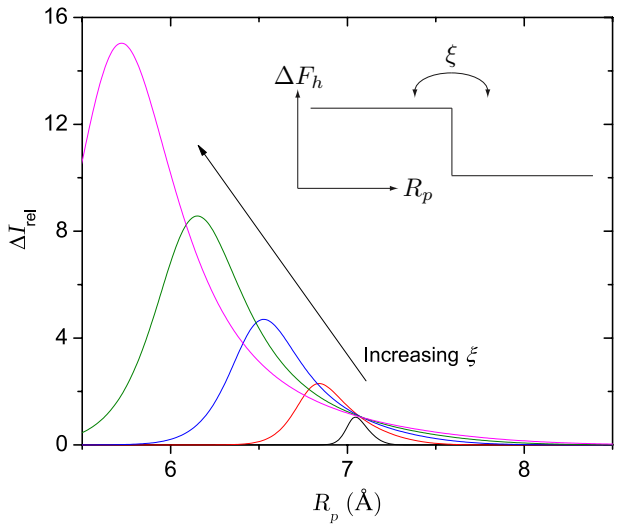

Figure 5.8: Relative current noise induced by structural fluctuations in the effective pore radius and/or hydration layer radius. The inset shows the approximate change in free energy ΔF_h as a function of effective pore radius in proximity to a hydration layer structure. The noise in the pore radius induces fluctuations between the high and low energy states. Here the third hydration layer radius of Cl^- is taken, $R_h = 7.1\,\text{Å}$. See the text for details on ΔF_h. The fluctuation strength from right to left is $\xi = 0.05,\ 0.15,\ 0.25,\ 0.35,\ 0.45\,\text{Å}$.

ion with a material of lower dielectric constant but in the exact geometry of the water molecules. This is very unlikely since the pore screening comes from the fixed surface of the pore and thus in a different functional form. Nevertheless, it is instructive to see how the drops in the current are reduced by this effective lowering of the energy barrier. Figures 5.9 and 5.10 show the energy barrier and current for several values of this effective dielectric constant. We find that even for fairly large ϵ_p (~ 7), the barriers are large enough to give a noticeable drop in the current.

Bulk concentration - We also mention the effect of changing the concentration of ions in bulk. We have assumed that the hydration layers are well formed away from the pore. Large ionic concentration in bulk, however, would affect the formation of the hydration layers. For a completely disassociated 1:1 salt, the ion-ion distance goes as $\sim 9.4/n_0^{1/3}$ Å where the bulk concentration, n_0, is given in mols/L. Thus, the inter-ion distance is $\sim 9.4\,\text{Å}$ for a 1 M solution, which is almost large enough to house both the first and second hydration layers. However,

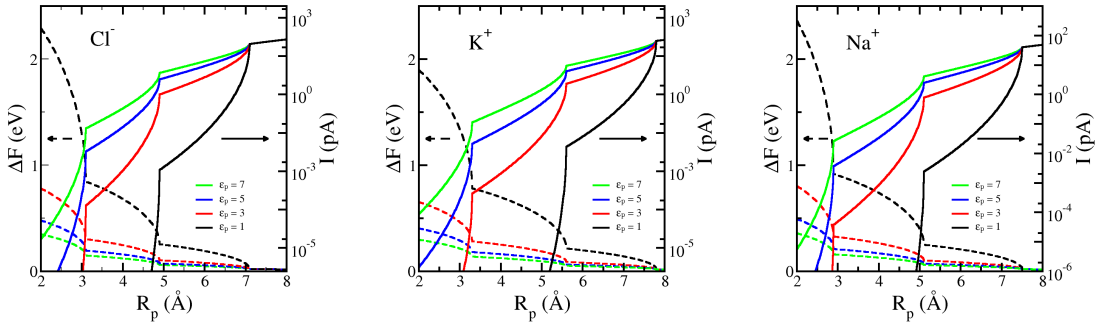

Figure 5.9: Free energy changes, ΔF, and currents versus the effective pore radius for the monovalent ions and several values of ϵ_p and for a field of $1\,\mathrm{mV/Å}$. The dashed lines indicate the free energy change. The solid lines indicate the current (see text for details). The currents are for $\epsilon_p = 7$, 5, 3, 1, from top to bottom.

concentrations lower than 1 M are preferable.

Some remarks - We have discussed many of the factors that will affect the detection of quantized ionic conductance. The most ideal experiment would be one with pores of well-controlled diameter and with smooth surfaces. Likewise, a small (or no) amount of surface charge and a low dielectric constant of the pore will make the effect more pronounced (and the ability to gate a pore, e.g., made of a nanotube, would help even more in understanding the energetics of transport). Not having these factors under control greatly affects the transport properties of the ions [108]. Therefore, pores made of, for instance, semiconducting nanotubes may be ideal. Indeed, pores made of these materials have been recently demonstrated [109]. However, rough surfaces that are present in pores made of, e.g., silicon nitride, should still allow for quantized conductance to be observed, so long as the variation of the effective radius of the pore is not too strong. The noise in the effective radius of the pore was investigated previously in Ref. [81], where we found that only beyond variation in the radius of $0.2 - 0.3\,\mathrm{Å}$ will the effect be washed out. However, even beyond this variation magnitude, the relative current noise signifies the presence of steps in the energy barrier, thus giving a more robust indicator of the hydration layers' effect on transport.

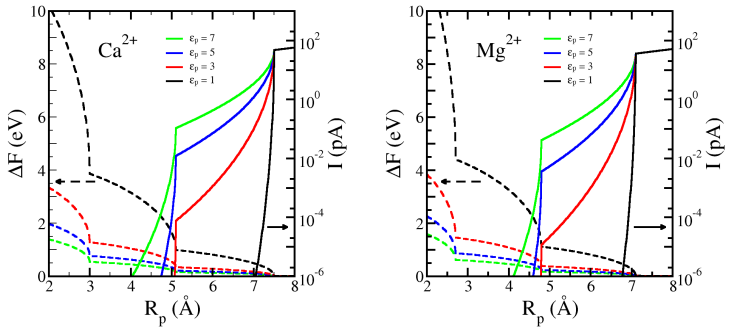

Figure 5.10: Free energy changes, ΔF, and currents versus the effective pore radius for the divalent ions and several values of ϵ_p and for a field of 1 mV/Å.The dashed lines indicate the free energy change. The solid lines indicate the current (see text for details). The currents are for $\epsilon_p = 7$, 5, 3, 1, from top to bottom.

5.6 Conclusions

Ionic transport in nanopores is a fascinating subject with a long history and impact in many areas of science and technology. Recent work on developing aqueous-based nanotechnology and understanding biological ion channels requires a firm understanding of how water and ions behave in confined geometries and under non-equilibrium conditions due to applied fields. For example, the quest for ultra-fast, single-molecule DNA sequencing has yielded a number of proposals based on nanopores [46]. Among them, transverse electronic transport [12, 11] (whose theoretical basis includes the investigation of atomistic fluctuations [12, 11, 49, 50] and electronic noise in liquid environments [51]) and ionic blockade [6, 55, 56, 57, 36, 58, 59, 60] have yielded promising recent experiments (Refs. [61, 62] and [63, 64], respectively). In all these cases, both water and ions are present and will have a significant impact on the signals and noise observed.

In this work, we have analyzed in detail the recent prediction of quantized ionic conductance [81] and examined how different aspects of the ion-nanopore system influence the detection of this phenomenon. Namely, we have shown that the ion type affects very little the radii at which the conduction should drop. High valency ions, however, should give even more pronounced drops in the current and thus may help in detecting this effect. Further, the presence of the hydration layers

gives a peak in the relative noise at pore radii congruent with a layer radius. This relative noise is much less sensitive to fluctuations than the average current, and provides a promising approach to detect the effect of hydration.

Overall, quantized ionic conductance yields experimental predictions that will shed light on the contribution of dehydration to ion transport and we hope this work will motivate experiments in this direction.

5.7 Acknowledgments

This research is supported by the U. S. Department of Energy through the LANL/LDRD Program (M. Z.) and by the NIH-NHGRI (J. W. and M. D.).

Chapter 5, is in part a reprint of the material as it appears in Michael Zwolak, James Wilson, and Massimiliano Di Ventra, "Dehydration and ionic conductance quantization in nanopores," *Journal of Physics: Condensed Matter* **22**, 45 (2010). The dissertation author was a co-author of this paper.

Chapter 6

Single-Base DNA Discrimination via Transverse Ionic Transport

6.1 Introduction

Measuring transverse *electronic* currents within a nanochannel to differentiate between DNA/RNA bases [11, 12, 13] is a promising new approach for sequencing DNA fast and at low cost. It consists of feeding a single-stranded DNA molecule through a channel equipped with nanometer-scale electrodes able to differentiate (via transverse electrical current) the electronic structure of the various bases as they pass by [11, 12, 13]. This approach has been recently realized in various experiments [14, 32, 33, 34, 35].

On the other hand, ionic current through a nanopore has been known for over a decade to be useful in detecting when a DNA translocation event has occurred [6, 36, 37, 38, 39, 40], and has even been able to give some information about the sequence [7, 8]. However, within a nanochannel, the ionic current blockaded by an arbitrary strand of DNA is a non-trivial convolution of a large number of blockade events from different bases [41], and as such it is difficult to sequence at the single base level with this physical mechanism, unless the bases are fed one at a time through the opening.

Recent advances in the fabrication of ionic nanochannels [17] have shown

that it is possible to use a pair of intersecting nanochannels to detect the transport of DNA. In that particular experiment a double stranded DNA has been translocated through one channel, while the ionic current flowing through the second, transverse, channel is modulated based on the presence or absence of DNA at the intersection. So far, fabrication techniques have only realized nanochannel widths of about 20 to 30 nanometers, still too large to be able to achieve single-base resolution, if at all possible. In fact, the linear dimension of an individual base is on the order of 1nm, so in order to distinguish a single base, channels of widths comparable to or less than 2nm are required. Even if those were possible to make, it is not at all obvious whether single-base discrimination would be achievable with transverse ionic transport.

Inspired by these experimental advances, and the possibility to realize devices with intersecting channels as those mentioned above, in this work we seek to determine whether changes in *transverse ionic conductance* are sufficient to discriminate the different DNA bases, were intersecting nanochannels of width comparable to or less than 2nm fabricated. To be more specific, the set up we have in mind is illustrated in Fig. 6.1. We place a strand of poly$(\mathrm{dX})_7$ where X is one of the bases A, C, G, T in the pore. To optimize the simulation time required, the single-stranded DNA (ss-DNA) is already placed inside of a Si_3N_4 nanopore of diameter of 1.8nm that runs along the y-axis. The simulation box has a regular hexagonal shape with an in-radius of 3.3nm in the x-y plane to correspond with hexagonal periodic boundary conditions. Intersecting this, a transverse pore of diameter 1.4nm extends in the z-axis direction. The membrane is 2.8nm thick in the z direction and the simulation box, which contains water stacked in the z direction, has rectangular periodicity in the z direction. In addition, an atom in the backbone of each of the outer two bases in the ss-DNA is fixed in space during the simulation. This allows the bases that are near the intersection of the pores to move without any constraint, but does not allow the DNA to move out of the pore or to fold up. Moreover, after each simulation run we vary the position of the two outermost bases along the y axis by 0.1Å, while also keeping the distance between the above two points fixed. This way the ionic currents we detect correspond to

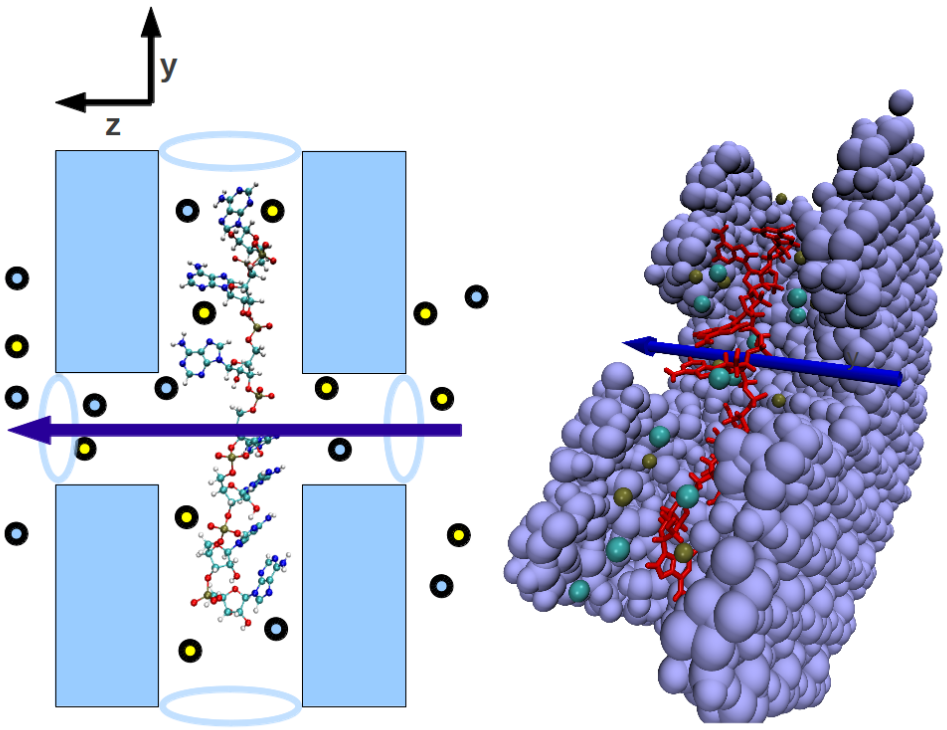

Figure 6.1: Schematic of two intersecting nanochannels. A strand of DNA lies along the longitudinal (vertical) pore. The ionic current flows in the transverse (horizontal) direction symbolized by the arrow.

different configurations of the single bases, facing the transverse channel. In fact, bases were found to shift several angstroms during the simulation while the end points remained fixed.

6.2 Simulation

An electric field is then imposed in the z-direction causing ions to flow through the transverse channel in the Si_3N_4. As has been discussed in [11] the electric field in the longitudinal and transverse directions can be independently manipulated to allow the DNA to translocate through the pore slowly, yet still have sufficient time to make measurements. Many measurements of current for each base can then be made, allowing a current *distribution* to be built for each

base as it passes the channel intersection.

The system is simulated using the molecular dynamics (MD) package NAMD [19]. It is solvated with 5nm of water on each side of the channel in the z-axis and K and Cl ions are added such that the molarity of the system is 2M [1]. We use periodic boundary conditions all around. The static energy is minimized and then the system is brought up to room temperature. Next, a Langevin piston is used to equilibrate at room temperature and 1 atmosphere of pressure in the NPT ensemble. Finally the system is run in the NVT ensemble with a Langevin damping term to keep the temperature steady. An electric field is applied transverse to the DNA such that the voltage drop across the cell in the z direction is 0.5V. The first 2ns are used as a further equilibration with the same conditions as the production run. During this first 2ns the system approaches a steady-state current (see also below).

In the previous work covering transverse *electronic* transport [11, 13], the current was calculated using a single-particle scattering approach [42]. The molecular dynamics simulated the structural fluctuations inherent in the water-pore system, and these fluctuations caused the variations in the current. That study was possible because the timescales in which the electronic transport occurred (due to tunneling) are much shorter than the timescales of the structural fluctuations. Unfortunately, the ionic transport timescales are much longer, so we must simulate many nanoseconds to correctly capture the fluctuations of the ionic current. For each base, 31 simulations were run. In all, we have simulated 1736ns of MD, with each simulation run of 14ns. The computational resources required to characterize the current distributions were significantly greater than in the electronic transport study. To accomplish this, we made use of a cluster of 30 dual-core nodes and 10 eight-core nodes. We also used computing time from the Open Science Grid project [43], scavenging time whenever resources were available.

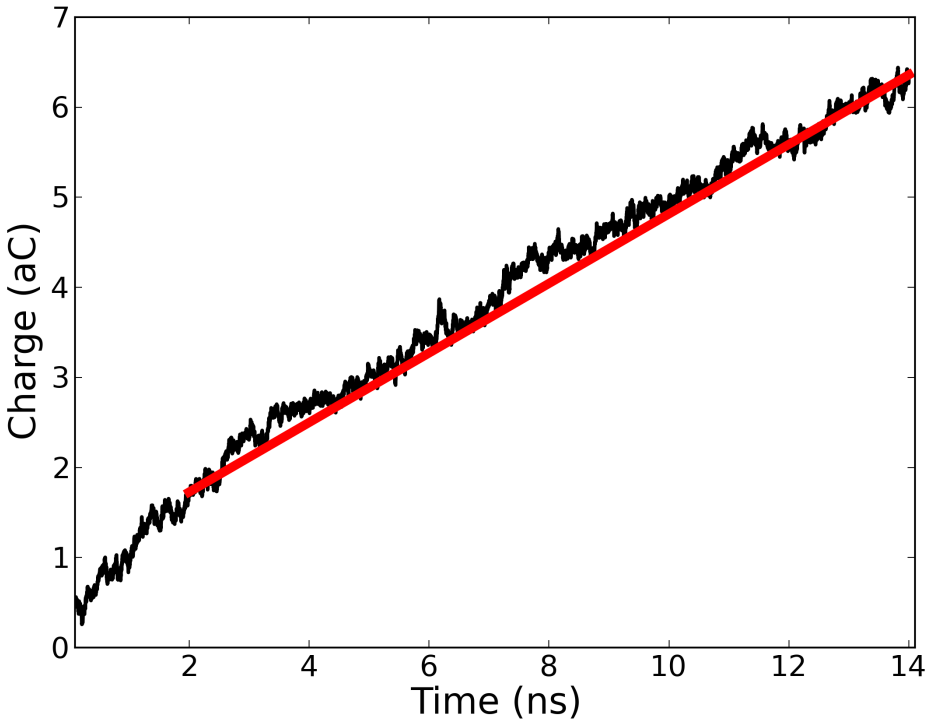

Figure 6.2: Typical plot of ionic current integrated over time, namely $\int_S dq$ where S is the surface area of the transverse channel. The slope of this curve is the instantaneous current at each time in units of nA. We have used an interval of time $\Delta t = 1$ ps. After about 2 ns a steady-state current sets in. Its value is obtained from the slope of the red line obtained from the last 12 ns of simulation. This particular plot is for poly(dA)$_7$.

6.3 Results

We calculate the current directly by looking at the motion of the ions in the system

$$I = \sum_i \frac{q_i \Delta z_i}{l_z \Delta t}, \tag{6.1}$$

where l_z is the cell length of the system, and the sum is over all ions in the system. Δz_i is the distance the ith ion has traveled in an interval of time Δt. Other methods of calculating the current were tested and they yielded similar results to equation (6.1). For instance, the slope of the curve $Q(t) = \int_S dq$ at steady state,

[1]The choice of a larger molarity than the typical 1M is again to reduce the already demanding computational requirements.

where S is the surface of the transverse channel (at steady state the choice of this surface is irrelevant [42]) yields similar currents.

In about 1 to 2 ns, the ions move into a steady-state current-carrying state, so we do not begin to calculate the current until after this time period. The next 12 ns are then used to calculate the current for that run. This short transient is clear from Fig. 6.2 where we plot $Q(t)$ for a typical run. Other, shorter, lengths of time were checked, but the best, most stable results were obtained with the present timescale. A rough estimate of the standard deviation of the current measurement is that it would scale as the inverse square root of the measurement window [44]. Experimental measurements for a reasonable sampling frequency would average over a longer timescale than we have simulated, so we expect the current distributions to be even less noisy than we have calculated. Our rate of 12 ns per sample would correspond to a sampling frequency of approximately 80MHz. Ionic current measurements have been recently conducted at 1MHz [45], which would be a factor of 80 slower than our simulations.

The current distributions from the all-atom MD simulations are shown in Fig 6.3. First we note, as was also done in the case of transverse electrical currents [11], that one measurement of ionic current is not sufficient to sequence a DNA strand to high precision. However, the distributions we have obtained are sufficiently disjoint to not require a large number of measurements per base. We calculate below the number of measurements required based on our data, but it goes without saying that each device (in terms of channel widths, shape, etc.) would likely produce its own set of probability distributions.

Second, the average current we obtain suggests the order $\bar{I}_G < \bar{I}_A < \bar{I}_C < \bar{I}_T$. Apart from C and T this order is in reasonable agreement with the order of volumes of the different nucleotides $V_G > V_A > V_T > V_C$ [46], suggesting that the currents are somewhat correlated with the exclusion volume of each base [46, 41]. However, as also indicated by the reverse order of C and T, the exclusion volume alone cannot fully explain the order of the average currents we have obtained, and other microscopic effects must also intervene such as the strength of the base dipoles, roughness of the surfaces at the channel intersection, and possibly other

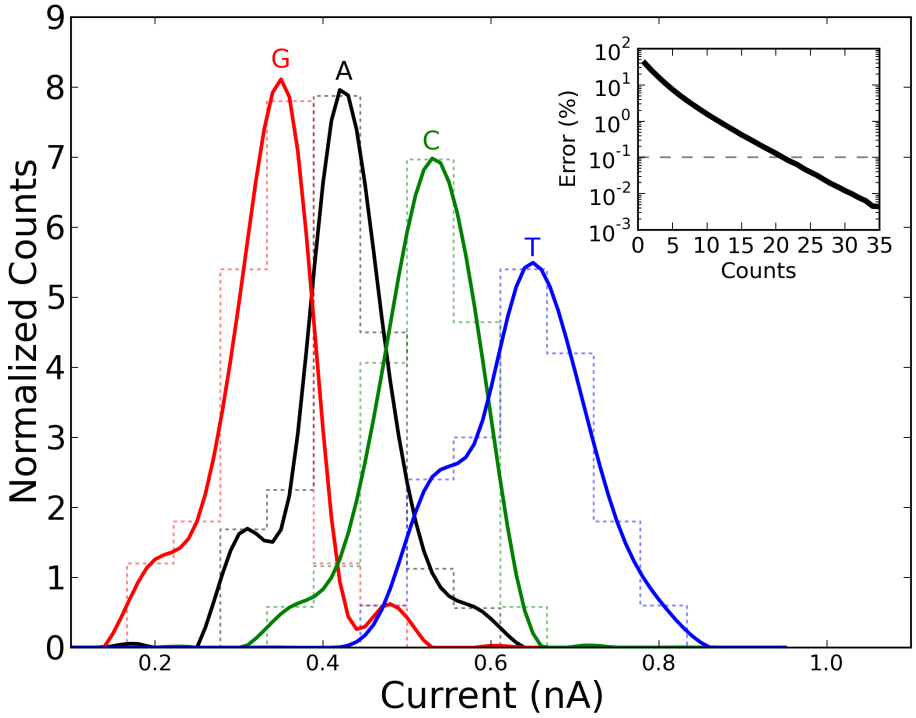

Figure 6.3: Transverse ionic current distributions for the different nucleotides in the pair of intersecting channels of Fig. 6.1. The inset shows the probability of identifying a base incorrectly after measuring the current for that base "counts" times.

ones. Again, this confirms that the actual distributions will likely depend on the structural properties of each device.

6.4 Analysis

In order to sequence with this particular approach, we then parallel the protocol suggested in Ref. [11] by one of us (MD). First, run a strand of DNA with known composition through the longitudinal channel, e.g., a homogeneous strand of the four different bases. Then, while the DNA is translocating through the channel, measure the current as many times as possible and build up a distribution of currents for each DNA base. Once this distribution for each base is obtained, the DNA strand that is to be read is sent through. The current is read N times

for each base X as it passes through the intersection, and each of those N readings is analyzed for the probability that it could be an A, C, T, or G. The probability of X being correctly identified after one measurement is given by [11]

$$\langle P_X(I)\rangle = \frac{n_X(I)}{n_A(I) + n_C(I) + n_T(I) + n_G(I)} \tag{6.2}$$

Where $n_X(I)$ is the height of the normalized distribution for current I, and X is one of the bases A, C, G, T.

After N measurements, the probability that the base at the intersection of the two channels is correctly identified is [11]

$$\langle P_X^N\rangle = \frac{\prod_i^N n_X(I_i)}{\sum_{J=A,C,G,T}\left(\prod_i^N n_J(I_i)\right)} \tag{6.3}$$

A Monte Carlo method was employed with the distribution data obtained from our simulations to calculate the probability of correctly identifying a base after N measurements. For each base, I_1 through I_N were randomly generated from the current distribution for that base. The probability P_X is then calculated from equation (6.3). Assuming an equal proportion of each of the bases within the strand being sequenced, the probability of correctly identifying a base at random after N independent measurements is just the average

$$P_N = \frac{1}{4}\left(P_A^N + P_C^N + P_G^N + P_T^N\right). \tag{6.4}$$

We then average over realizations to arrive at the probability, $P = \langle P_N\rangle$, that we correctly identify a random base after N measurements.

In the inset of figure 6.3, we plot a graph of uncertainty, $E = 1 - P$, in identifying bases versus number of independent measurements. When at least 20 measurements are taken, the probability of error is less than 0.1%. This seems to suggest that, with these particular distributions, we need fewer measurements with this method than with transverse electronic transport for the same error rate [11]. However, as already noted ionic transport measurements are typically slower than electronic ones. Nevertheless, if we measure the ionic current at a reasonable

rate of 100kHz, then DNA could be identified at $5,000$ bases per second using this scheme. Therefore, an entire genome could be sequenced in less than 7 days without parallelization. Clearly, this estimate may be somewhat off according to the actual distributions obtained experimentally. Furthermore, the error rate assumes that the pore is made small enough that neighboring bases do not affect the current, and that it is easy to tell when a base passes over the intersection. If that is not the case, it may take several more measurements per base simply to know that a change in base at the intersection has occurred. These effects would all increase the number of measurements required.

6.5 Conclusions

We conclude that the approach we have described in this paper can indeed discriminate between the four DNA bases and has thus potential as an alternative sequencing method. Furthermore, this method would easily lend itself to parallelism. For example, a device dedicated to each chromosome would decrease the time required to sequence an entire genome by a factor of ten. Finally, this same idea could be implemented as a protocol for protein sequencing. We are now in the process of assessing the feasibility of this last possibility.

6.6 Acknowledgment

This research has been partially supported by the NIH-National Human Genome Research Institute. We also gratefully acknowledge discussions with M. Ramsey. Part of the calculations in this work were performed by using resources provided by the Open Science Grid, which is supported by the National Science Foundation and the U.S. Department of Energy.

Chapter 6 is in part a reprint of the material as it appears in James Wilson and Massimiliano Di Ventra, "Single-Base DNA Discrimination via Transverse Ionic Transport," *Nanotechnology* **24** 415101 (2013). The dissertation author was the primary author of this paper.

Chapter 7

Simulating a Battery by Using the Microcanonical Formalism

Microcanonical formalism [27, 28, 29] provides another method of probing nano-scale transport. All methods of extracting current characteristics from systems must make simplifying assumptions because of the intractability of the many-body quantum mechanical problem. This formalism explores transport characteristics of nanoscale objects by calculating accurately, the time-dependent quantum mechanics of the local system. However, it simplifies the battery-lead system to relatively small capacitive leads. Because a battery-lead system is generally very large, and a local nanoscale system can be just a few atoms, the computational complexity can be reduced greatly, so that it can be solved numerically by any of the normal quantum mechanical methods.

This approach differs from Landauer Formalism [110, 111, 112], which abstracts the concept of the battery and leads as merely supplying electrons with a given momentum and energy to the system. The electrons scatter off of the junction, and the transmission percentage determines the current through the device. This is a time-independent process, and a steady-state is forced on the system by assumption.

The microcanonical formalism defines a method of probing current in which the system is completely time-dependent, and a quasi-steady state appears in the system naturally. It easily includes interactions, and this depends only on the

method used to simulate a closed quantum mechanical system. Thus, because of the different assumptions made, the microcanonical picture is more suited to certain types of problems [113] where we are interested in various interactions, time correlations, and where the geometry of the system can be more easily approximated by a finite reservoir.

One of the difficulties of the microcanonical formalism, is the limited time within which the simulation approximates a larger, macroscopic system. The system requires a time τ_{SS} to set up a steady state that is relatively short. Then the quasi steady-state breaks down in another time scale τ_{BD} which is related to the amount of time for electrons to bounce off of the edges of the system and interfere with themselves. Thus, this time scale τ_{BD} is proportional to the length of the system, and inversely proportional to the fermi velocity of the electrons. The time between τ_{SS} and τ_{BD} is the time after a quasi steady-state has been set up, and serves as an approximation to a global steady-state observed in an extended system. To extend this useful time, it is then necessary to increase τ_{BD} because τ_{SS} is relatively short and does not change easily.

The Stochastic Schrodinger Equation (SSE)[114] is a method that can be used to simulate an open quantum system [31]. It can be integrated directly, but it can also be combined with TDDFT [115, 116] to decrease the computational complexity. Each realization of the SSE provides an individual trajectory, however the average trajectory is what is physical. Thus, with many realizations of the system, we have the ability to inspect the noise which the bath produces. However, one must perform many of these realizations to recover the average, long term dynamics of the system. Other methods such as solving the Lindblad equation only provide the average dynamics (or most probable realization) but are generally cheaper computationally to solve.

This work seeks to simulate a battery within the microcanonical formalism to reach longer timescales than would normally be allowed by the system size. We do this by applying a specially designed bath that mimics the function of a battery in a circuit to a model system (1D chain). We choose to use a 1D chain as the model system for simplicity and ease of computation, and we likewise use a

tight-binding method for ease of computation.

This model system starts with an excess charge on one end, and then over the time τ_{BD} discharges through the atoms of interest. A battery's function in this case would be to take electrons from the side that has low potential energy, and place them back onto the high potential energy side. We approximate this effect by applying a bath that continually projects each electron back into an earlier, charged state. This bath is simply the projection operator, and only has one parameter, which is the characteristic time. Some consideration is given for optimizing this parameter below.

Thus the scheme is to take the stochastic Schrodinger equation:

$$d\Psi = \left[-i\hat{\mathbf{H}}\Psi - \frac{1}{2}\hat{\mathbf{S}}^{\dagger}\hat{\mathbf{S}}\Psi\right]dt + \hat{\mathbf{S}}\Psi dW \tag{7.1}$$

With a $\hat{\mathbf{S}}$ operator that projects into an earlier state Ψ_0, such that

$$\hat{\mathbf{S}} = \frac{1}{\sqrt{\gamma}}|\Psi_0\rangle\langle\Psi_0| \tag{7.2}$$

Because we are measuring the current by dq/dt, care must be taken to not include the movement of the charge by the $\hat{\mathbf{S}}$ operator. Referencing Figure 7.1, the terms of the SSE that contain the $\hat{\mathbf{S}}$ operator move the electrons from the right side of the system to the left side by way of an external battery. This movement of electrons should not be thought of as an electron current going through the system, instead, it is a movement of electrons from the right side into a fictional reservoir. Electrons are then injected from a reservoir into the left side of the system. We are measuring the current through the center of the system, and must not include the movement of the electrons due to the last two terms of the SSE, as they do not cross the center. The deterministic portion of the SSE (the first term on the RHS) is then moving electrons from left to right across the measurement point. This subtle point can be satisfied if we evolve the system in a two step process: first evolve the system according to the first term on the RHS, measure the current due to this process, then add in the effect of the last two terms. The evolution of the system is identical to the normal Euler-Maruyama method, but the current measurement only takes into account the first term on the RHS.

The microcanonical formalism allows many methods of solving the Schrodinger equation, including solving a discretized system, using a tight-binding model, or even using DFT. We use the tight-binding model in this work to take advantage of the reduced computational complexity. In this simulation, we model N sites representing a 1D chain of N gold atoms. We use$t_i = t$ as the transmission coefficient between nearest neighbors in the chain, and set the transmission coefficient to zero for any non-adjacent pair of sites. Thus the Hamiltonian is expressed as the following:

$$\hat{\mathbf{H}} = -t \sum_{i=1}^{N} \left(c_{i-1}^{\dagger} c_i + c_i^{\dagger} c_{i+1} \right) + \sum_{i=1}^{N} V_i c_i^{\dagger} c_i \tag{7.3}$$

Where V_i is the externally applied potential measured at the ith site.

We initialize the system following the methods of [28]. We start by using an initial Hamiltonian $\hat{\mathbf{H}}_{\mathbf{0}}$ by setting V_i to be some constant $-V/2$ where $i < N/2$, and where $i \geq N/2$ to be $+V/2$. By diagonalizing this hamiltonian, we have N ground state wavefunctions of electrons in the system. For half-filling, we take the $N/2$ lowest energy wavefunctions, and these wavefunctions are then propagated using a Hamiltonian such that $V_i = 0$.

We used a 0.2V potential difference for the initial conditions for most runs, as this was a good compromise to decrease numerical errors in the simulation. Some deterministic runs were done to determine how the system scales with N and t. The simulation achieved a steady-state in a time of approximately 2.5a.u. regardless of the size of the system. The time to set up the steady-state depends primarily on the value of the transmission constant t. However, the time that the system took to break down, scaled linearly with the number of sites in the system N. With $N = 32$, the time τ_{BD} is approximately 15a.u. while $\tau_{BD} = 30$ for $N = 64$.

In a break junction, the difference in potential is localized at the break, which corresponds to the center of our system. We are then interested in the current passing that break, so we calculate the current in the center of the system. To calculate the current at the $N/2$th site, we calculate the total charge in the right half of the system at each time step. The derivative of this charge, dN/dt, gives the instantaneous current in the center of the system. This is dependent on the

closed nature of the system, i.e. there is no leakage of charge out from the edges of the system. Furthermore, because the Hamiltonian only includes nearest neighbor interactions, during one timestep, electron density can only travel a maximum of 1 site away. Thus we can look at just one site instead of the whole right half of the system. In essence, we just need to look at the flux at each timestep between site $N/2$ and site $N/2+1$. This serves to decrease the number of calculations required to calculate the current, and also decreases the numerical error in calculating the current when the current is a small number.

The conductance of this system is measured to be $G_0 = 2e^2/h$ which is in accordance with the 1 channel conductance for a Landauer calculation. This conductance is stable under a wide range of potential differences, and numbers of sites. Having recovered the correct value of G_0 for the conductance in the system, we can proceed knowing the simulation is working correctly.

The system is then opened up to the bath by adding a stochastic term to the simulation. Because we are using a projection operator as the $\hat{\mathbf{S}}$ operator, we must choose the state(s) that we are projecting into, and we must choose the strength of the operator by setting the timescale γ. First, we look at the state to project the system into. The goal is to provide a recharging of the system, so the first choice could be projecting into the initial state of the system. This state, however is not immediately a current carrying state. A small amount of time (2a.u.) lapses before it reconfigures into a current carrying steady-state. The goal is to be in a current carrying steady-state indefinitely as when a battery is connected to the circuit. Therefore, rather than projecting into the initial state, we project into a state that has just reached the steady-state.

Our scheme then takes two phases. We first evolve the system forward in time using the deterministic Schrodinger equation until the system reaches a quasi steady-state. The state at this point we will call state A. Next, we evolve the system using the stochastic Schrodinger equation with the $\hat{\mathbf{S}}$ operator. The $\hat{\mathbf{S}}$ takes the form of a projection operator pointing back to state A. We now only have one parameter to choose, and that is the strength of the stochastic term. The task is to make γ small enough that the system does not move beyond the

steady-state behavior, but large enough that the system is not frozen into the initial state. In the limit as $\gamma \to 0$, the stochastic term dominates and the system is essentially always in the initial state. To determine the optimal value for γ, we ran simulations for varying values of γ and Figure 7.2 compares the results.

We then must choose this time to be short enough that electrons are not reaching the edge of the system, but we must choose it to not be so short that the dynamics are frozen. We must also not choose it to be too long. When this parameter goes to infinity, that corresponds to the limiting case where the bath does not act on the system, and it is identical to the deterministic Schrodinger equation. When this time goes to zero, the stochastic term in the equation dominates, and the state variable stays in its initial configuration and phase, with only a fluctuating magnitude (which on average is equal to unity). This latter limit is much more difficult to numerically converge because the stochastic term scales as the square root of dt when using the Euler-Maruyama integrator. When the stochastic term is small, the deterministic portion of the equation dominates, and scales as dt.

The parameter γ has units of time, and represents a timescale over which the initial wavefunction is diluted out of the simulation. For instance, if we prepare the system with a wave packet on the left side of the system, with a sufficiently small γ, the wave packet will never reach the right side of the system. One can then tune the system via γ such that the packet can reach an arbitrary distance within the system. After testing various γ values, we see that the system "sees" approximately 4γ ahead in time such that if it would normally take the wave packet Xa.u. to reach the other side, if we set $\gamma \leq X/4$, the packet will never reach the other side.

In our model system with $N = 32$ sites, we have from $t = 2.5$ to $t = 15$ that the system is in a quasi-steady state. We then create a bath that mimics a battery by using the stochastic Schrodinger equation. Because the stochastic term disturbs the dynamics, we want to find the weakest stochasticity that will still extend the quasi-steady state indefinitely. Thus, we choose to implement the bath starting at the beginning of the quasi-steady state, leaving the maximum time before the

system breaks down. The quasi steady state breaks down $12.5a.u.$ after this time in the deterministic system, so we will choose $\gamma \leq 12.5/4$. Figure 7.2 shows the effect of γ on the system. With large γ there is only a slight forcing back to A, and the graph follows that of the deterministic system closely. As γ decreases, the system deviates less from the steady state, until $\gamma = 2.8$, and $\gamma = 1.6$ approximate a system that is being fully recharged continuously by a battery.

Each realization represents one trajectory out of an ensemble, and a single realization is not physically meaningful, the average of the ensemble is what is meaningful. By performing a large number of realizations, we can find the statistics of that ensemble, which we can use to estimate how many realizations must be performed to converge the variables of interest. In our case, we look specifically at the current. Specifically, we look at the ensemble of currents at a specified time t_1. The standard deviation $\sigma(t_1)$ converges quite quickly (within a few hundred realizations). However, because it may be quite large, $\mu(t_1) = I(t_1)$ requires on the order of a thousand realizations to converge, and it converges as the square root of the number of realizations.

For relatively large γ, the standard deviation of the current varies inversely with γ. Therefore for $\gamma = 1.6$ more realizations are needed than for $\gamma = 25$. For the simulations in this work, between 1000 and 3000 realizations were run. In exchange for that computational cost, however, the simulation can run indefinitely, and the simulations are embarrassingly parallel. This work was done on an 80 core Xeon cluster, but with little work could be used with highly parallel systems such as GPU clusters.

Using an open quantum system approach, we submit a method of extending the microcanonical formalism to allow for longer simulations with small system sizes. With a sufficiently strong and carefully constructed bath, we show that a 1D model system can reach arbitrarily long timescales without the quasi-steady state breaking down. This can be another tool in seeking to understand nano-scale transport.

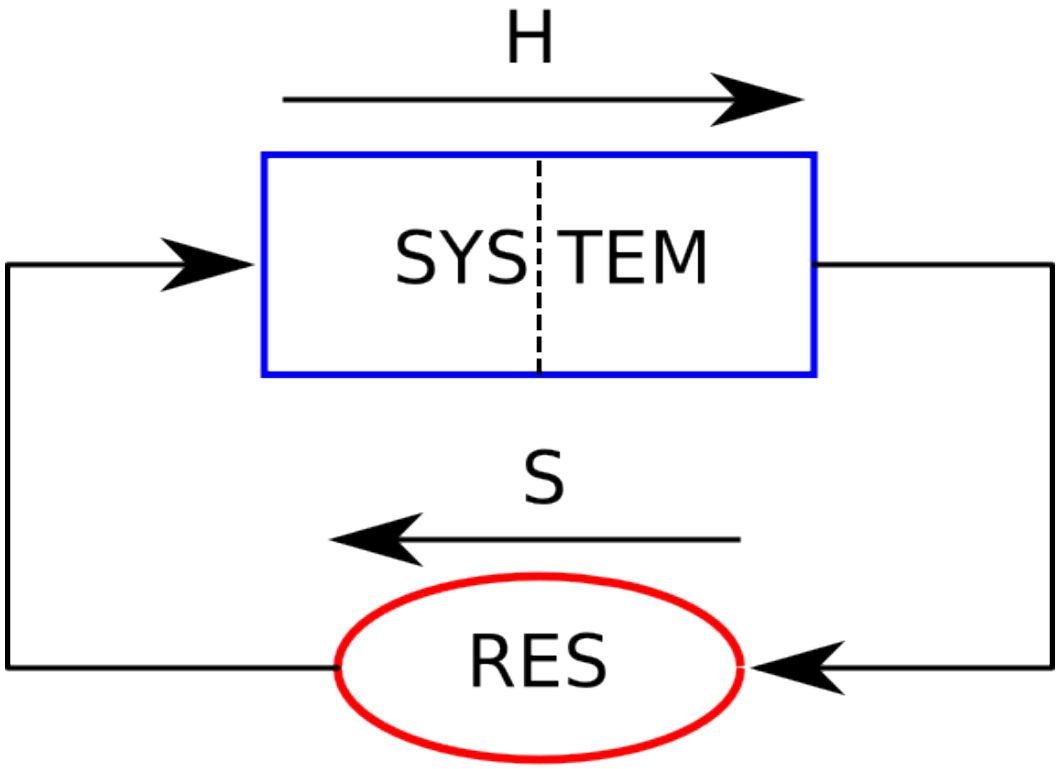

Figure 7.1: (Color online)Schematic of the system under study. An externally applied potential gradient causes a greater density of electrons on the left. Then when the potential gradient is removed, the electrons are pushed to the right. The current is measured in the center of the system (denoted by a vertical dashed line). Once electrons have been displaced to the right, the stochastic terms, which include the $\hat{\mathbf{S}}$ operator, move electrons from right to left in the system. However, the stochastic terms do not move electrons past the vertical dashed line, but rather around through a fictional reservoir RES.

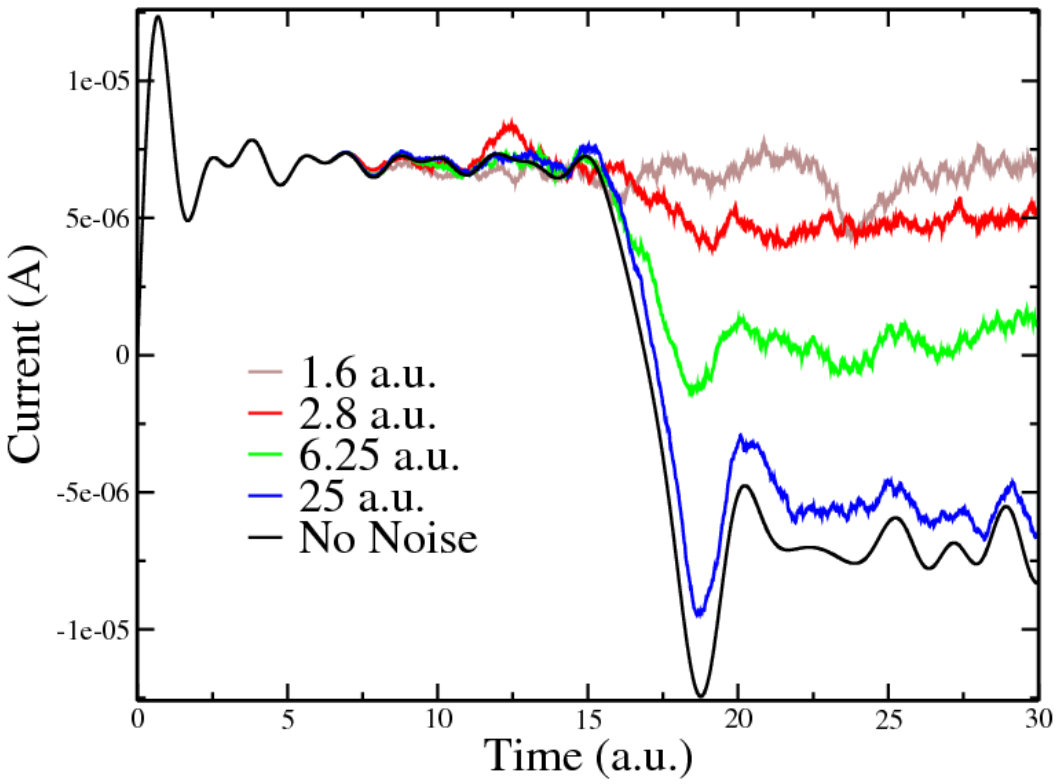

Figure 7.2: (Color online)Current in a 1D system with a tight-binding model consisting of $N = 32$ sites and using the stochastic Schrodinger equation. Each curve represents a different strength of the stochastic term, with smaller numbers corresponding to faster action and thus stronger stochastic component. The strengths are, from top to bottom, 1.6, 2.8, 6.25, and 25 a.u. All stochastic curves initiate at $T = 6.5$a.u. The bottom curve corresponds to zero stochastic component.

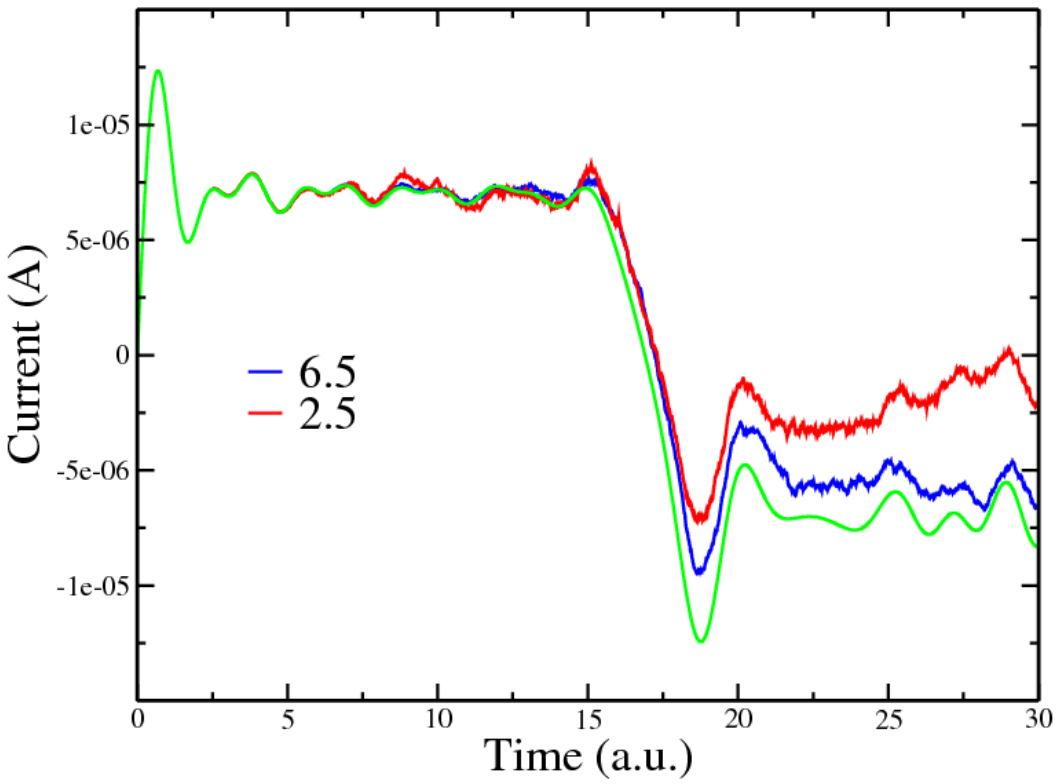

Figure 7.3: (color online) Current in a 1D system with a tight-binding model consisting of $N = 32$ sites and using the stochastic Schrodinger equation. Both stochastic curves have the same amount of noise strength $\gamma = 25$a.u. The top curve initiates at $T = 2.5$a.u. The middle curve initiates at $T = 6.5$a.u. and the bottom curve is not stochastic.

Bibliography

[1] James D Watson, Francis HC Crick, et al. Molecular structure of nucleic acids. *Nature*, 171(4356):737–738, 1953.

[2] Fred Sanger and Alan R Coulson. A rapid method for determining sequences in dna by primed synthesis with dna polymerase. *Journal of molecular biology*, 94(3):441–448, 1975.

[3] F. Sanger, S. Nicklen, and A. R. Coulson. Dna sequencing with chain-terminating inhibitors. *Proc. Natl. Acad. Sci. U. S. A.*, 74:5463, 1977.

[4] Eric S. Lander et al. Initial sequencing and analysis of the human genome. *Nature (London, U. K.)*, 409:860, 2001.

[5] Michael Zwolak, Johan Lagerqvist, and Massimiliano Di Ventra. Quantized ionic conductance in nanopores. *Physical review letters*, 103(12):128102, 2009.

[6] John J. Kasianowicz, Eric Brandin, Daniel Branton, and David W. Deamer. Characterization of individual polynucleotide molecules using a membrane channel. *Proc. Natl. Acad. Sci. U. S. A.*, 93:13770, 1996.

[7] Ian M Derrington, Tom Z Butler, Marcus D Collins, Elizabeth Manrao, Mikhail Pavlenok, Michael Niederweis, and Jens H Gundlach. Nanopore dna sequencing with mspa. *Proceedings of the National Academy of Sciences*, 107(37):16060–16065, 2010.

[8] Elizabeth A Manrao, Ian M Derrington, Andrew H Laszlo, Kyle W Langford, Matthew K Hopper, Nathaniel Gillgren, Mikhail Pavlenok, Michael Niederweis, and Jens H Gundlach. Reading dna at single-nucleotide resolution with a mutant mspa nanopore and phi29 dna polymerase. *Nature biotechnology*, 30(4):349–353, 2012.

[9] Stefan W Kowalczyk, David B Wells, Aleksei Aksimentiev, and Cees Dekker. Slowing down dna translocation through a nanopore in lithium chloride. *Nano letters*, 12(2):1038–1044, 2012.

[10] Utkur Mirsaidov, Jeffrey Comer, Valentin Dimitrov, Aleksei Aksimentiev, and Gregory Timp. Slowing the translocation of double-stranded dna using a nanopore smaller than the double helix. *Nanotechnology*, 21(39):395501, 2010.

[11] J. Lagerqvist, M. Zwolak, and M. DiVentra. Fast DNA sequencing via transverse electronic transport. *Nano Lett.*, 6(4):779, 2006.

[12] Michael Zwolak and Massimiliano Di Ventra. Electronic signature of DNA nucleotides via transverse transport. *Nano Lett.*, 5:421, 2005.

[13] Matt Krems, Michael Zwolak, Yuriy V Pershin, and Massimiliano Di Ventra. Effect of noise on dna sequencing via transverse electronic transport. *Biophysical journal*, 97(7):1990–1996, 2009.

[14] Takahito Ohshiro, Kazuki Matsubara, Makusu Tsutsui, Masayuki Furuhashi, Masateru Taniguchi, and Tomoji Kawai. Single-molecule electrical random resequencing of dna and rna. *Scientific reports*, 2, 2012.

[15] Jiali Li, Derek Stein, Ciaran McMullan, Daniel Branton, Michael J Aziz, and Jene A Golovchenko. Ion-beam sculpting at nanometre length scales. *Nature*, 412(6843):166–169, 2001.

[16] A. J. Storm, J. H. Chen, X. S. Ling, H.W. Zandbergen, and C. Dekker. Fabrication of solid-state nanopores with single-nanometre precision. *Nat. Mater.*, 2(8):537, 2003.

[17] Laurent D Menard, Chad E Mair, Michael E Woodson, Jean Pierre Alarie, and J Michael Ramsey. A device for performing lateral conductance measurements on individual double-stranded dna molecules. *ACS nano*, 6(10):9087–9094, 2012.

[18] William L Jorgensen, Jayaraman Chandrasekhar, Jeffry D Madura, Roger W Impey, and Michael L Klein. Comparison of simple potential functions for simulating liquid water. *The Journal of chemical physics*, 79:926, 1983.

[19] James C. Phillips, Rosemary Braun, Wei Wang, James Gumbart, Emad Tajkhorshid, Elizabeth Villa, Christophe Chipot, Robert D. Skeel, Laxmikant Kalé, and Klaus Schulten. Scalable molecular dynamics with namd. *J. Comput. Chem.*, 26(16):1781, 2005.

[20] William Humphrey, Andrew Dalke, and Klaus Schulten. Vmd: visual molecular dynamics. *Journal of molecular graphics*, 14(1):33–38, 1996.

[21] N. Foloppe and A. D. MacKerell. All-atom empirical force field for nucleic acids: I. parameter optimization based on small molecule and condensed phase macromolecular target data. *J. Comput. Chem.*, 21(2):86, 2000.

[22] A. D. MacKerell and N. K. Banavali. All-atom empirical force field for nucleic acids: Ii. application to molecular dynamics simulations of DNA and RNA in solution. *J. Comput. Chem.*, 21(2):105, 2000.

[23] R. Grun. Crystal-structure of beta-si3n4 - structural and stability considerations between alpha-si3n4 and beta-si3n4. *Acta Crystallographica Section B-Structural Science*, 35(APR):800, 1979.

[24] Chuen Ho, Rui Qiao, Jiunn B Heng, Aveek Chatterjee, Rolf J Timp, Narayana R Aluru, and Gregory Timp. Electrolytic transport through a synthetic nanometer-diameter pore. *Proceedings of the National Academy of Sciences of the United States of America*, 102(30):10445–10450, 2005.

[25] Min Jun Kim, Ben McNally, Kazuyoshi Murata, and Amit Meller. Characteristics of solid-state nanometre pores fabricated using a transmission electron microscope. *Nanotechnology*, 18(20):205302, 2007.

[26] Philippe Cluzel, Anne Lebrun, Christoph Heller, Richard Lavery, Jean-Louis Viovy, Didier Chatenay, François Caron, et al. Dna: an extensible molecule. *SCIENCE-NEW YORK THEN WASHINGTON-*, pages 792–794, 1996.

[27] M. Di Ventra and T.N. Todorov. Transport in nanoscale systems: the microcanonical versus grand-canonical picture. *Journal of Physics: Condensed Matter*, 16(45):8025, 2004.

[28] Neil Bushong, Na Sai, and Massimiliano Di Ventra. Approach to steady-state transport in nanoscale conductors. *Nano Letters*, 5(12):2569–2572, 2005.

[29] N. Sai, N. Bushong, R. Hatcher, and M. Di Ventra. Microscopic current dynamics in nanoscale junctions. *Physical Review B*, 75(11):115410, 2007.

[30] Pierre Gaspard and M Nagaoka. Non-markovian stochastic schrödinger equation. *The Journal of chemical physics*, 111:5676, 1999.

[31] H. Appel and M. Di Ventra. Stochastic quantum molecular dynamics. *Physical Review B*, 80(21):212303, 2009.

[32] Aleksandar P Ivanov, Emanuele Instuli, Catriona M McGilvery, Geoff Baldwin, David W McComb, Tim Albrecht, and Joshua B Edel. Dna tunneling detector embedded in a nanopore. *Nano letters*, 11(1):279–285, 2010.

[33] Xiaogan Liang and Stephen Y Chou. Nanogap detector inside nanofluidic channel for fast real-time label-free dna analysis. *Nano letters*, 8(5):1472–1476, 2008.

[34] Shuai Chang, Shuo Huang, Jin He, Feng Liang, Peiming Zhang, Shengqing Li, Xiang Chen, Otto Sankey, and Stuart Lindsay. Electronic signatures of all four dna nucleosides in a tunneling gap. *Nano letters*, 10(3):1070–1075, 2010.

[35] Makusu Tsutsui, Kazuki Matsubara, Takahito Ohshiro, Masayuki Furuhashi, Masateru Taniguchi, and Tomoji Kawai. Electrical detection of single methylcytosines in a dna oligomer. *Journal of the American Chemical Society*, 133(23):9124–9128, 2011.

[36] David W. Deamer and Daniel Branton. Characterization of nucleic acids by nanopore analysis. *Acc. Chem. Res.*, 35:817, 2002.

[37] Christopher A Merchant, Ken Healy, Meni Wanunu, Vishva Ray, Neil Peterman, John Bartel, Michael D Fischbein, Kimberly Venta, Zhengtang Luo, AT Charlie Johnson, et al. Dna translocation through graphene nanopores. *Nano letters*, 10(8):2915–2921, 2010.

[38] Slaven Garaj, W Hubbard, A Reina, J Kong, D Branton, and JA Golovchenko. Graphene as a subnanometre trans-electrode membrane. *Nature*, 467(7312):190–193, 2010.

[39] Grégory F Schneider, Stefan W Kowalczyk, Victor E Calado, Grégory Pandraud, Henny W Zandbergen, Lieven MK Vandersypen, and Cees Dekker. Dna translocation through graphene nanopores. *Nano letters*, 10(8):3163–3167, 2010.

[40] Stefan Howorka and Zuzanna Siwy. Nanopore analytics: sensing of single molecules. *Chemical Society Reviews*, 38(8):2360–2384, 2009.

[41] Daniel Branton, David W Deamer, Andre Marziali, Hagan Bayley, Steven A Benner, Thomas Butler, Massimiliano Di Ventra, Slaven Garaj, Andrew Hibbs, Xiaohua Huang, et al. The potential and challenges of nanopore sequencing. *Nature biotechnology*, 26(10):1146–1153, 2008.

[42] M. Di Ventra. *Electrical Transport in Nanoscale Systems*. Cambridge University Press, 2008.

[43] Ruth Pordes, Don Petravick, Bill Kramer, Doug Olson, Miron Livny, Alain Roy, Paul Avery, Kent Blackburn, Torre Wenaus, Frank Würthwein, et al. The open science grid. In *Journal of Physics: Conference Series*, volume 78, page 012057. IOP Publishing, 2007.

[44] Aleksei Aksimentiev. Deciphering ionic current signatures of dna transport through a nanopore. *Nanoscale*, 2(4):468–483, 2010.

[45] Jacob K Rosenstein, Meni Wanunu, Christopher A Merchant, Marija Drndic, and Kenneth L Shepard. Integrated nanopore sensing platform with sub-microsecond temporal resolution. *Nature methods*, 9(5):487–492, 2012.

[46] Michael Zwolak and Massimiliano Di Ventra. Colloquium: Physical approaches to DNA sequencing and detection. *Rev. Mod. Phys.*, 80(1):141, 2008.

[47] Bertil Hille. *Ion Channels of Excitable Membranes*. Sinauer Associates, Sunderland, 2001.

[48] F. M. Ashcroft. *Ion channels and disease*. Academic Press, San Diego, 2000.

[49] Johan Lagerqvist, Michael Zwolak, and Massimiliano Di Ventra. Influence of the environment and probes on rapid DNA sequencing via transverse electronic transport. *Biophys. J.*, 93(7):2384, 2007.

[50] Johan Lagerqvist, Michael Zwolak, and Massimiliano Di Ventra. Comment on "characterization of the tunneling conductance across DNA bases". *Phys. Rev. E*, 76:013901, 2007.

[51] Matt Krems, Michael Zwolak, Yuriy V. Pershin, and Massimiliano Di Ventra. Effect of noise on dna sequencing via transverse electronic transport. *Biophys. J.*, 97(7):1990, 2009.

[52] Jiunn Benjamin Heng, Aleksei Aksimentiev, Chuen Ho, Valentin Dimitrov, Thomas W. Sorsch, John F. Miner, William M. Mansfield, Klaus Schulten, and Gregory Timp. Beyond the gene chip. *Bell Labs Technical Journal*, 10(3):5, 2005.

[53] Maria E. Gracheva, Anlin Xiong, Aleksei Aksimentiev, Klaus Schulten, Gregory Timp, and Jean-Pierre Leburton. Simulation of the electric response of DNA translocation through a semiconductor nanopore-capacitor. *Nanotechnology*, 17(3):622, 2006.

[54] Maria E Gracheva, Aleksei Aksimentiev, and Jean-Pierre Leburton. Electrical signatures of single-stranded DNA with single base mutations in a nanopore capacitor. *Nanotechnology*, 17:3160, 2006.

[55] Mark Akeson, Daniel Branton, John J. Kasianowicz, Eric Brandin, and David W. Deamer. Microsecond time-scale discrimination among polycytidylic acid, polyadenylic acid, and polyuridylic acid as homopolymers or as segments within single RNA molecules. *Biophys. J.*, 77:3227, 1999.

[56] David W. Deamer and Mark Akeson. Nanopores and nucleic acids: prospects for ultrarapid sequencing. *Trends Biotechnol.*, 18:147, 2000.

[57] Wenonah Vercoutere, Stephen Winters-Hilt, Hugh Olsen, David Deamer, David Haussler, and Mark Akeson. Rapid discrimination among individual DNA hairpin molecules at single-nucleotide resolution using an ion channel. *Nat. Biotechnol.*, 19:248, 2001.

[58] Wenonah Vercoutere and Mark Akeson. Biosensors for DNA sequence detection. *Curr. Opin. Chem. Biol.*, 6(6):816, 2002.

[59] Wenonah A. Vercoutere, Stephen Winters-Hilt, Veronica S. DeGuzman, David Deamer, Sam E. Ridino, Joseph T. Rodgers, Hugh E. Olsen, Andre Marziali, and Mark Akeson. Discrimination among individual watson-crick base pairs at the termini of single DNA hairpin molecules. *Nucleic Acids Res.*, 31(4):1311, 2003.

[60] Stephen Winters-Hilt, Wenonah Vercoutere, Veronica S. DeGuzman, David Deamer, Mark Akeson, and David Haussler. Highly accurate classification of watson-crick basepairs on termini of single DNA molecules. *Biophys. J.*, 84:967, 2003.

[61] Makusu Tsutsui, Masateru Taniguchi, Kazumichi Yokota, and Tomoji Kawai. Identifying single nucleotides by tunnelling current. *Nat Nano*, 5:286, 2010.

[62] Shuai Chang, Shuo Huang, Jin He, Feng Liang, Peiming Zhang, Shengqing Li, Xiang Chen, Otto Sankey, and Stuart Lindsay. Electronic signatures of all four dna nucleosides in a tunneling gap. *Nano Lett.*, 10:1070, 2010.

[63] James Clarke, Hai-Chen Wu, Lakmal Jayasinghe, Alpesh Patel, Stuart Reid, and Hagan Bayley. Continuous base identification for single-molecule nanopore dna sequencing. *Nat Nano*, 4(4):265, 2009.

[64] David Stoddart, Andrew J. Heron, Ellina Mikhailova, Giovanni Maglia, and Hagan Bayley. Single-nucleotide discrimination in immobilized dna oligonucleotides with a biological nanopore. *Proc. Natl. Acad. Sci. U. S. A.*, 106(19):7702, 2009.

[65] Declan A. Doyle, João Morais Cabral, Richard A. Pfuetzner, Anling Kuo, Jacqueline M. Gulbis, Steven L. Cohen, Brian T. Chait, and Roderick MacKinnon. The structure of the potassium channel: Molecular basis of k+ conduction and selectivity. *Science*, 280(5360):69, 1998.

[66] Shin-Ho Chung, Olaf S. Anderson, and Vikram V. Krishnamurthy. *Biological Membrane Ion Channels: Dynamics, Structure, and Applications*. Springer, New York, 2007.

[67] Michael Thomas, Dylan Jayatilaka, and Ben Corry. The predominant role of coordination number in potassium channel selectivity. *Biophys. J.*, 93(8):2635, 2007.

[68] Sameer Varma and Susan B. Rempe. Tuning ion coordination architectures to enable selective partitioning. *Biophys. J.*, 93(4):1093, 2007.

[69] Philip W. Fowler, Kaihsu Tai, and Mark S. P. Sansom. The selectivity of k+ ion channels: Testing the hypotheses. *Biophys. J.*, 95(11):5062, 2008.

[70] Todor Dudev and Carmay Lim. Determinants of k+ vs na+ selectivity in potassium channels. *J. Am. Chem. Soc.*, 131(23):8092, 2009.

[71] David L. Bostick and Charles L. Brooks. Selectivity in k+ channels is due to topological control of the permeant ion's coordinated state. *Proc. Natl. Acad. Sci. U. S. A.*, 104(22):9260, 2007.

[72] Haibo Yu, Sergei Yu Noskov, and Benot Roux. Hydration number, topological control, and ion selectivity. *J. Phys. Chem. B*, 113(25):8725, 2009.

[73] David L. Bostick and Charles L. Brooks. Statistical determinants of selective ionic complexation: Ions in solvent, transport proteins, and other hosts. 96(11):4470, 2009.

[74] Jiali Li, Derek Stein, Ciaran McMullan, Daniel Branton, Michael J. Aziz, and Jene A. Golovchenko. Ion-beam sculpting at nanometre length scales. *Nature (London, U. K.)*, 412:166, 2001.

[75] Scott A. Miller, Vaneica Y. Young, and Charles R. Martin. Electroosmotic flow in template-prepared carbon nanotube membranes. *J. Am. Chem. Soc.*, 123(49):12335, 2001.

[76] Jason K. Holt, Aleksandr Noy, Thomas Huser, David Eaglesham, and Olgica Bakajin. Fabrication of a carbon nanotube-embedded silicon nitride membrane for studies of nanometer-scale mass transport. *Nano Lett.*, 4(11):2245, 2004.

[77] Zuzanna Siwy, Elizabeth Heins, C. Chad Harrell, Punit Kohli, and Charles R. Martin. Conical-nanotube ion-current rectifiers: The role of surface charge. *J. Am. Chem. Soc.*, 126(35):10850, 2004.

[78] C. Chad Harrell, Punit Kohli, Zuzanna Siwy, and Charles R. Martin. Dna, nanotube artificial ion channels. *J. Am. Chem. Soc.*, 126(48):15646, 2004.

[79] Jason K. Holt, Hyung Gyu Park, Yinmin Wang, Michael Stadermann, Alexander B. Artyukhin, Costas P. Grigoropoulos, Aleksandr Noy, and Olgica Bakajin. Fast mass transport through sub-2-nanometer carbon nanotubes. *Science*, 312(5776):1034, 2006.

[80] Cees Dekker. Solid-state nanopores. *Nat Nano*, 2(4):209, 2007.

[81] Michael Zwolak, Johan Lagerqvist, and Massimiliano Di Ventra. Quantized ionic conductance in nanopores. *Phys. Rev. Lett.*, 103(12):128102, 2009.

[82] Massimiliano Di Ventra. *Electrical Transport in Nanoscale Systems.* Cambridge University Press, Cambridge, 2008.

[83] Adrian Parsegian. Energy of an ion crossing a low dielectric membrane: Solutions to four relevant electrostatic problems. *Nature*, 221:844, 1969.

[84] V. Adrian Parsegian. Ion-membrane interactions as structural forces. *Ann. N. Y. Acad. Sci.*, 264(Carriers and Channels in Biological Systems):161, 1975.

[85] Alexander A. Rashin and Barry Honig. Reevaluation of the born model of ion hydration. *J. Phys. Chem.*, 89(26):5588, 1985.

[86] Benoît Roux, Hsiang Ai Yu, and Martin Karplus. Molecular basis for the born model of ion solvation. *J. Phys. Chem.*, 94(11):4683, 1990.

[87] Yizhak Marcus. Thermodynamics of solvation of ions. part 5.gibbs free energy of hydration at 298.15 k. *J. Chem. Soc., Faraday Trans.*, 87(18):2995, 1991.

[88] D. G. Levitt. Electrostatic calculations for an ion channel. i. energy and potential profiles and interactions between ions. *Biophys. J.*, 22(2):209, 1978.

[89] Peter C. Jordan. Energy barriers for passage of ions through channels : Exact solution of two electrostatic problems. *Biophys. Chem.*, 13(3):203, 1981.

[90] P. C. Jordan. Electrostatic modeling of ion pores - energy barriers and electric-field profiles. *Biophys. J.*, 39(2):157, 1982.

[91] Benoît Roux, Toby Allen, Simon Bernéche, and Wonpil Im. Theoretical and computational models of biological ion channels. *Q. Rev. Biophys.*, 37(1):15, 2004.

[92] S. Teber. Translocation energy of ions in nano-channels of cell membranes. *J. Stat. Mech.*, ,:P07001, 2005.

[93] J. Zhang, A. Kamenev, and B. I. Shklovskii. Conductance of ion channels and nanopores with charged walls: A toy model. *Phys. Rev. Lett.*, 95:148101, 2005.

[94] A. Kamenev, J. Zhang, A.I. Larkin, and B.I. Shklovskii. Transport in one-dimensional coulomb gases: From ion channels to nanopores. *Physica A*, 359:129, 2006.

[95] Alan Finkelstein and Olaf Sparre Andersen. The gramicidin a channel: a review of its permeability characteristics with special reference to the single-file aspect of transport. *The Journal of membrane biology*, 59(3):155–171, 1981.

[96] Joao H. Morais-Cabral, Yufeng Zhou, and Roderick MacKinnon. Energetic optimization of ion conduction rate by the k+ selectivity filter. *Nature*, 414(6859):37, 2001.

[97] J. D. Jackson. *Classical Electrodynamics*. Wiley, 3rd edition, 1998.

[98] A. H. Narten. Liquid water: Atom pair correlation functions from neutron and x-ray diffraction. *J. Chem. Phys.*, 56(11):5681, 1972.

[99] Hitoshi Ohtaki and Tamás Radnai. Structure and dynamics of hydrated ions. *Chem. Rev.*, 93:1157, 1993.

[100] Lu Yang and Shekhar Garde. Modeling the selective partitioning of cations into negatively charged nanopores in water. *J. Chem. Phys.*, 126:084706, 2007.

[101] Anna Ignaczak, J. A. N. F. Gomes, and M. N. D. S. Cordeiro. Quantum and simulation studies of $X^{-}(H_2O)_n$ systems. *Electrochim. Acta*, 45:659, 1999.

[102] H. Kistenmacher, H. Popkie, and E. Clementi. Study of the structure of molecular complexes. viii. small clusters of water molecules surrounding li+, na+, k+, f, and cl ions. *J. Chem. Phys.*, 61(3):799, 1974.

[103] Chen Song and Ben Corry. Intrinsic ion selectivity of narrow hydrophobic pores. *J. Phys. Chem. B*, 113(21):7642, 2009.

[104] B. Neumcke and P. Läuger. Nonlinear electrical effects in lipid bilayer membranes: Ii. integration of the generalized nernst-planck equations. *Biophys. J.*, 9(9):1160, 1969.

[105] R. S. Eisenberg, M. M. Klosek, and Z. Schuss. Diffusion as a chemical reaction: Stochastic trajectories between fixed concentrations. *J. Chem. Phys.*, 102(4):1767, 1995.

[106] D. G. Luchinsky, R. Tindjong, I. Kaufman, P. V. E. McClintock, and R. S. Eisenberg. Self-consistent analytic solution for the current and the access resistance in open ion channels. *Phys. Rev. E*, 80(Copyright (C) 2010 The American Physical Society):021925, 2009.

[107] Matt Krems, Yuriy V. Pershin, and Massimiliano Di Ventra. Ionic memcapacitive effects in nanopores. *arXiv:1001.0796*, 2010.

[108] Eduardo R. Cruz-Chu, Aleksei Aksimentiev, and Klaus Schulten. Ionic current rectification through silica nanopores. *J. Phys. Chem. C*, 113(5):1850, 2009.

[109] Haitao Liu, Jin He, Jinyao Tang, Hao Liu, Pei Pang, Di Cao, Predrag Krstic, Sony Joseph, Stuart Lindsay, and Colin Nuckolls. Translocation of single-stranded dna through single-walled carbon nanotubes. *Science*, 327(5961):64, 2010.

[110] R. Landauer. Spatial variation of currents and fields due to localized scatterers in metallic conduction. *IBM Journal of Research and Development*, 1(3):223–231, 1957.

[111] M. Büttiker, Y. Imry, R. Landauer, and S. Pinhas. Generalized many-channel conductance formula with application to small rings. *Phys. Rev. B*, 31:6207–6215, May 1985.

[112] M. Büttiker. Four-terminal phase-coherent conductance. *Physical review letters*, 57(14):1761–1764, 1986.

[113] G. Vignale and M. Di Ventra. Incompleteness of the landauer formula for electronic transport. *Physical Review B*, 79(1):014201, 2009.

[114] NG Van Kampen. *Stochastic Processes in Physics and Chemistry*. North-Holland, 2007.

[115] M. Di Ventra and R. DAgosta. Stochastic time-dependent current-density-functional theory. *Physical review letters*, 98(22):226403, 2007.

[116] R. DAgosta and M. Di Ventra. Stochastic time-dependent current-density-functional theory: A functional theory of open quantum systems. *Physical Review B*, 78(16):165105, 2008.